Catena 226 (2023) 107050

Contents lists available at ScienceDirect

Catena

journal homepage: www.elsevier.com/locate/catena

Rainfall erosivity variability over the United States associated with large-scale climate variations by El Niño/southern oscillation

Jai Hong Lee [a,*], Pierre Y. Julien [b], Jongseok Cho [b], Seungho Lee [c], Jungho Kim [d], Woochul Kang [e]

[a] Department of Engineering, South Carolina State University, Orangeburg, SC, USA
[b] Department of Civil and Environmental Engineering, Colorado State University, Fort Collins, CO 80523, USA
[c] South Carolina Lexington H. School, Lexington, SC, USA
[d] First Street Foundation, Brooklyn, NY, USA
[e] Department of Land, Water and Environment Research, Korea Institute of Civil Engineering and Building Technology (KICT), Goyang, Republic of Korea

ARTICLE INFO

Keywords:
Rainfall erosivity
Teleconnection
Southern Oscillation
ENSO

ABSTRACT

A comprehensive investigation of the contiguous Unites States rainfall erosivity patterns in relation to the warm and cold phases of El Niño/southern Oscillation (ENSO) was described using a set of empirical and statistical analyses, such as harmonic analysis, annual cycle composites, and cross-correlation analysis. Monthly rainfall erosivity index (REI) composites for the first harmonic, covering 24-month ENSO events, are formed for all climate divisions over the United States spanning up to 29 ENSO episodes. From the harmonic vectorial maps plotted on the study area, each vector reveals both intensity and temporal phase of the ENSO-related REI teleconnection, and the corresponding candidate and core regions are determined using a machine learning technique of Gaussian Mixture Model (GMM) based on magnitude and temporal phase of climate signal, and Köppen climate classification. As a result of vectorial mapping, five core regions were designated as the northwest (NW), the north central (NC), the northeast coastal (NEC), the southeast (SE), and the southwest/middle-inland (SWM) regions. During fall (0) to spring (+) seasons, the results of this analysis show negative (positive) rainfall erosivity response to the El Niño events at the NW and NC regions (NEC, SE, and SWM regions), while the opposite patterns are detected for the cold phase of ENSO. The temporal consistency values were 0.62 to 0.86 (0.73 to 0.82), and spatial coherence values ranged from 0.93 to 0.98 (0.94 to 0.97) for the El Niño (La Niña) events. Comparative analyses of rainfall erosivity responses to both warm and cold ENSO events reveal the high significance level of the ENSO-REI correlation with an opposite tendency in monthly rainfall erosivity anomalies. Above normal rainfall erosivity anomalies during the El Niño thermal forcing are more significant than below normal rainfall erosivity departures during the La Niña events. Consequently, middle latitude rainfall erosivity responses to the El Niño and La Niña phenomena are detectable over the contiguous United States.

1. Introduction

The El Niño/Southern Oscillation (ENSO) is a combined phenomenon of fluctuating sea surface temperature and atmospheric circulation over the central and eastern Pacific Ocean. It has a critical influence on climate patterns all over the world (WMO, 2014). These large-scale naturally occurring phenomena have been investigated at regional and global scale since the extreme phases of the ENSO episodes can cause major hydrologic extremes, e.g., floods and droughts, in various parts throughout the world. Many scientific approaches for understanding these phenomena in association with hydroclimatic parameters such as precipitation, temperature, streamflow, rainfall erosivity, etc., have been providing us a chance to prepare for the disastrous natural hazards.

Walker (1923), Walker and Bliss (1932) studied firstly the impacts of the Southern Oscillation (SO) on the Indian rainfall variability. Since then, a number of global scale studies related to the ENSO extreme phases showed various notable climatic links between hydroclimatic variable patterns and either phase of these opposite extreme events in many areas throughout the globe. Since Berlage (1966) found the ENSO extreme events correlated well with precipitation anomaly on a global basis, Rasmusson and Carpenter (1983) related the precipitation and temperature patterns to the extreme phase of Southern Oscillation and identified a significant link between the two variations. Also, Ropelewski and Halpert (1987, 1989) investigated temporal and spatial ranges showing consistent response of the climatic pattern over a variety

* Corresponding author.
E-mail address: june.lee@colostate.edu (J.H. Lee).

https://doi.org/10.1016/j.catena.2023.107050
Received 30 September 2022; Received in revised form 14 February 2023; Accepted 26 February 2023
Available online 20 March 2023

Nomenclature

List of Acronyms

(AI)	Artificial Intelligence
(CDF)	Cumulative Density Function
(DJF)	December-February
(ENSO)	El Niño/Southern Oscillation
(GMM)	Gaussian Mixture Model
(GEV)	Generalized Extreme Value
(ITS)	Index Time Series
(JJA)	June-August
(MAM)	March-May
(NCEI)	National Center for Environmental Information
(NOAA)	National Oceanic and Atmospheric Administration
(NC)	North Central
(NEC)	Northeast Costal
(NW)	Northwest
(PNA)	Pacific North American
(SLP)	Sea Level Pressure
(SON)	September-November
(SE)	Southeast
(SWM)	Southwest/middle-inland
(SO)	Southern Oscillation
(SOI)	Southern Oscillation Index
(SPI)	Standard Precipitation Index

of areas throughout the world to the extreme phases of the ENSO episodes and showed significant correlations of the ENSO forcing and continental climatic patterns, which were also identified by Kiladis and Diaz (1989). More recently, Westra et al. (2013) used generalized extreme value (GEV) to identify trends in annual maximum daily climate anomalies on a global basis and found a significant correlation with near-surface air temperature averaged globally.

On a regional basis, many studies found plausible evidence of the ENSO far-reaching effect on the low and mid latitude climate variabilities as documented by Douglas and Englehart (1981), Rasmusson and Wallace (1983), Ropelewski and Halpert (1986), Redmond and Koch (1991), and Kahya and Dracup (1994). For midlatitude regions, several studies indicated the ENSO–related hydroclimatic correlation. In the southeastern United States, Douglas and Englehart (1981) revealed that the extreme ENSO forcing modulated the increases of the seasonal precipitation. Ropelewski and Halpert (1986) studied the climatic links between the extreme southern oscillation and precipitation anomalies over North America and showed the ENSO-related hydroclimatic signals. This finding was also confirmed by Kiladis and Diaz (1989). Kahya and Dracup (1993, 1994) documented the influences of tropical thermal forcing on streamflow patterns of the United States focusing on extra-tropical teleconnections triggered by equatorial Pacific sea surface temperature anomalies. The western US streamflow responses to the North Pacific air-sea fluctuations were discussed by Diaz and Kiladis (1993), Redmond and Koch (1991), and Cayan and Peterson (1989). Chiew et al. (1994) documented the influence of the extreme phases of SO on streamflow variability over southeastern Australia using monthly streamflow data. In Turkey, some coherent regions where streamflow anomaly is statistically correlated with the extreme phases of ENSO events were founded by Kahya and Karabörk (2001). Korea-Japan precipitation patterns were investigated by Jin et al. (2005) in relation to the ENSO far-reaching effects. They used lead-lag correlation analysis for five categorized Southern Oscillation Index (SOI) and non-exceedance probability time series and showed evidence of the ENSO-related hydroclimatic correlation. In Sri Lanka, the Kelani River basin was examined by Chandimala and Zubair (2007) focusing on the streamflow probability related to the ENSO events and sea surface temperature using principal component and correlation analyses. Lee and Julien (2017) showed teleconnection of the extreme phases of ENSO forcing and midlatitude streamflow variability in the Korean peninsula, and Wang et al. (2020) investigated the role of ENSO events in climatic links between Chinese climatic patterns and tropical cyclones.

For predicting the amount of soil erosion, REI is considered as a more accountable indicator than rainfall amount itself. Severe storm events with high rainfall intensity modulate increase of soil erosion in that heavier storm has more energy to erode soil than lighter storm. REI can be used as a feasible hydroclimatic determinant for potential soil erosion risk caused by climate fluctuations. Many numerical studies about REI-based soil erosion have been documented throughout the globe including Nearing (2001), Nearing et al. (2004), Zhang et al. (2005), Shiono et al. (2013), Plangoen et al. (2013), Yang et al. (2015), Mohammadi (2015), Hoomehr et al. (2015), and Mondal et al. (2016). Nearing (2001) described analytical results of the rainfall erosivity variation and showed that increase of soil loss can be attributed to climate change. Yang et al. (2003) emphasized that the potential risk of soil erosion might significantly increase by climate change in the future. Nearing et al. (2004) examined rainfall erosivity as an important indicator for assessing the potential soil loss associated with climate change. Zhang et al. (2005) analyzed long-term annual mean REI data for two types of climate change scenarios for predicting expected soil erosion risk over the Yellow River basin and concluded rainfall erosivity increases significantly by climate change.

Previous studies on the ENSO-related teleconnection have more focused on the warm phase of extreme events and the impacts of the cold phase of extreme events have less scientific attention since the latter is considered less distinct and causes less disastrous natural hazards than the former. There has been rarely discussed in the literature about the teleconnections with a focus on comparative analysis and interpretation between the warm and cold phases of ENSO forcing. This study fills this gap by examining potential two ENSO driven rainfall erosivity anomalies in terms of degree of magnitude and temporal phase shift of the far-reaching impacts. As described in the relevant literature, many previous studies concentrated on global or rather broad regional scale analyses. Despite the various research on the ENSO-related climate teleconnection, little is known about the perspective of the ENSO forcing on the sub-regional rainfall erosivity variability. While studies over a broader area like the global or continental scale areas may yield good results, such results become too general and difficult to be implemented practically and tend to miss out localized climate variations. Therefore, delving into the underlying influences of the extreme phases of climatic variation on various scopes of rainfall erosivity patterns provides a constructive way to predict and prepare unexpected natural hazards. Thus, it is important to investigate systematically how the warm and cold phases of extreme ENSO events influence the sub-regional rainfall erosivity patterns over the United States. Recently, more comprehensive information about spatial and temporal variability of hydrometeorological parameters is being asked by potential users of the climate information as they are modulated by the extreme phases of ENSO forcing. Prior literature investigated the teleconnection between the extreme phases of Southern Oscillation and hydroclimatic anomalies over the United States using the observational data from 1931 to 1980 period (50 years) covering only 11 ENSO episodes (Ropelewski and Halpert, 1986). However, we recently experienced noticeably severe extreme ENSO episodes including strong El Niño events in 1982, 1997, 2015 and strong La Niña events in 1988, 1999, 2010, and so on. This study is to provide updated climate information of the temporal phase, spatial extent, and intensity of ENSO-related hydroclimatic signals at each of several locations over the proposed study area using updated long-term data

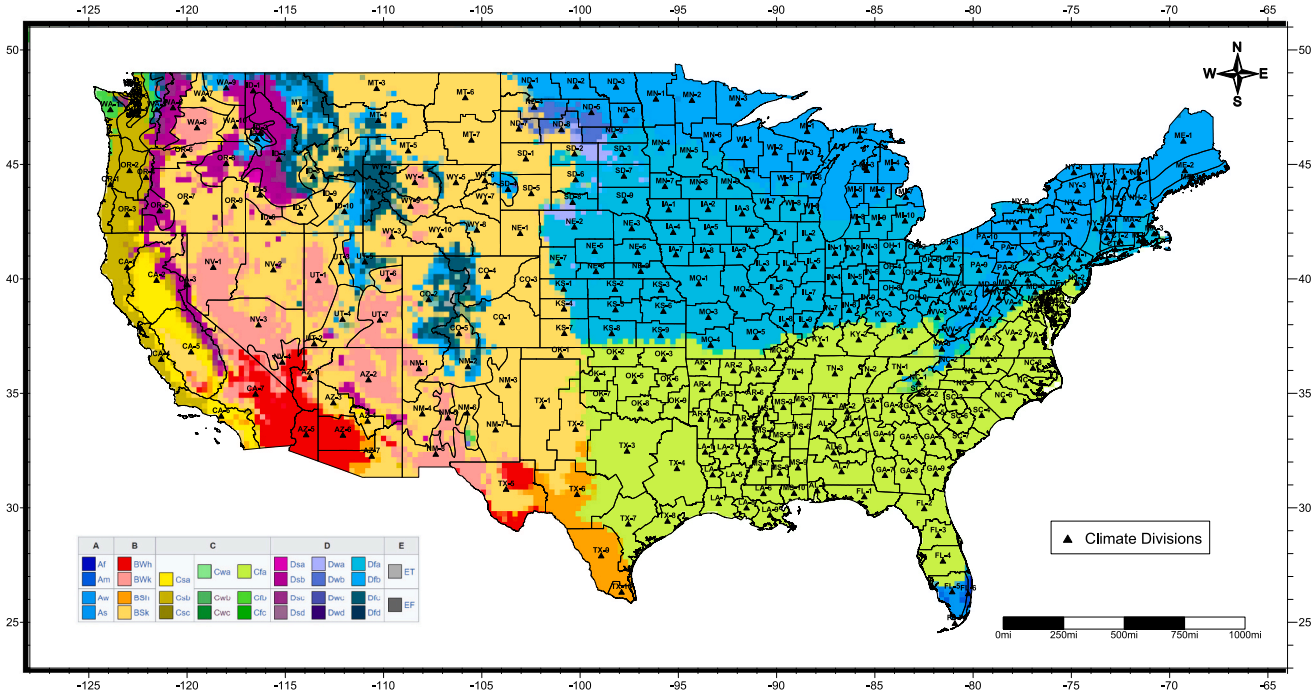

Fig. 1. Climate divisions and Köppen climate classification.

(1985–2020) spanning up to 29 ENSO episodes. In addition, from the perspective of methodological approaches, the previous studies including Ropelewski and Halpert (1986, 1987) used a subjective zoning method for determining core regions based on visual inspection over the harmonic dial maps. This subjective graphical approach implies that the ENSO-related hydrometeorological variability may include some uncertainties caused by other factors. In the present study, to categorize more objectively the candidate and core regions associated with the extreme phases of the ENSO forcing, an AI (Artificial Intelligence) machine learning technique was employed for determining the ENSO-related rainfall erosivity signal areas.

The main purpose of this study is to investigate rainfall erosivity patterns over the United States associated with warm and cold phases of ENSO events, i.e., El Niño and La Niña, using composite and harmonic analyses. This study uses an improved description by temporal cycle and spatial outlook for the intensity, time shift, and areal boundary of the ENSO-related REI correlation. Also, the present study compares the two types of teleconnections induced by El Niño and La Niña considering magnitude and trend of the significant responses, using annual cycle and cross-correlation analyses.

2. Data

Rainfall amount, intensity, and duration are the driving factors accounting for the rainfall erosivity index (REI). The REI time series are calculated for each monthly interval as follows:

$$REI_j = \sum_{k=1}^{m_j} (EI_{30})_k, \quad E = \sum_{r=1}^{n} 0.29\left(1 - 0.72e^{-0.082 i_r}\right)\Delta P_r$$

m_j is total number of erosive events during a given month j (=1, 2, …,12), k is index number of each event with its corresponding erosivity, EI_{30} is rainfall erosivity value of an individual event (MJ mm/ha/h), E is total energy for a storm (MJ/ha), i_r is rainfall intensity for each time interval (mm/h), ΔP_r is rainfall amount for the r th period (mm), r is an index for periods during a rainstorm where intensity can be considered to be constant, and n is number of periods. For monthly REI time series, U.S. 15-minute precipitation data and monthly climate division data were employed covering all climate regions over the contiguous United States. The source of the applied dataset is National Center for Environmental Information (NCEI) which is a governmental organization under the National Oceanic and Atmospheric Administration (NOAA). NOAA monitors and operates the overall United States meteorology. As shown in Fig. 1 and Table 1, the monthly climate division data cover the contiguous United States and range from 1895 to 2020 covering the overall ENSO episodes (29 El Niño and 22 La Niña).

Table 1
List of the ENSO episode years included in this study.

El Niño years	La Niña years
1905, 1911, 1914, 1918, 1923, 1925, 1930, 1932, 1939, 1941, 1951, 1953, 1957, 1963, 1965, 1969, 1972, 1976, 1982, 1986, 1991, 1994, 1997, 2002, 2004, 2006, 2009, 2015, 2018.	1910, 1915, 1917, 1924, 1928, 1938, 1950, 1955, 1964, 1971, 1973, 1975, 1985, 1988, 1995, 1998, 2000, 2005, 2007, 2010, 2011, 2017

To identify a consistent far-reaching effect of ENSO events on rainfall erosivity anomaly over the United States, two sets of extreme ENSO episodes are selected considering a comprehensive scope of criteria defined by Ropelewski and Halpert (1987, 1989), Rasmusson and Carpenter (1983), and Kiladis and Diaz (1989). The ENSO years for the two phases of extreme events selected in the present analysis are listed in Table 1. Southern Oscillation Index (SOI) is applied as an indicator of representing large-scale climate variation over the central-eastern Pacific Ocean (ENSO). This present analysis applied the SOI data calculated and recorded by the NOAA Climate Prediction Center. These SOI time series are computed based on the difference of the standardized sea level pressure (SLP) anomaly between Tahiti and Darwin, Australia.

3. Method

To examine the spatiotemporal extent to which El Niño/La Niña affect REI patterns over the United States, an empirical method (Ropelewski and Halpert, 1986), annual cycle and cross correlation analyses are employed with some changes and additions. As shown in Fig. 2, the

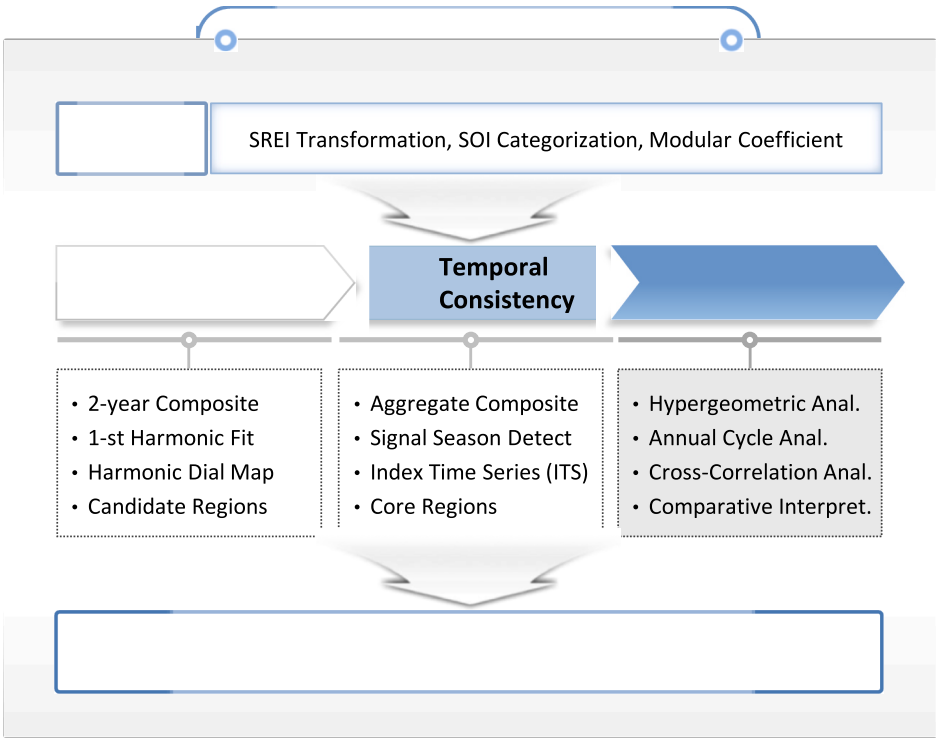

Fig. 2. Flowchart of the empirical methodology.

specific procedure of this analysis consists of mainly three steps, namely, data processing, spatial and temporal analyses, and comparative statistical assessment. In the first step, the original raw data are transformed into appropriate data formats, e.g., ranked percentile, modular coefficients, and categorized SOIs. In the second step, candidate and core regions are determined using composite and harmonic analyses. Then, in the last step, El Niño/La Niña–related REI signals are compared using lag cross-correlation and annual cycle analyses.

Monthly REI data over the United States are fitted to a gamma distribution for calculating the Standardized Rainfall Erosivity Index (SREI) using a standardized method developed by McKee et al. (1993), which is recommended by World Meteorological Organization (WMO, 2012). This is a probability index based on a statistical fit to an appropriate probability density function and a transformation into standardized normal distribution. The fitted distribution can be transformed into a cumulative density function (CDF) of the standardized normal distribution by the equal-probability conversion technique as shown in Fig. 3. The SREI time series, which have a mean of zero and standard deviation of unity, are used in the composite and harmonic analyses. Monthly REI time series are transformed into modular coefficients for carrying out annual cycle analysis. These modular coefficients remove the effects of dispersed variance and mean values. The REI data are expressed as percentages for the annual mean values. The modular coefficient data are calculated by the rate of each monthly REI value to the monthly average value for the entire data. It places all divisions on a same cycle with unchangeable condition of the cyclic feature of the values at the same time. In this present study, lag cross-correlation coefficients are computed for REI data and categorized SOI time series on a seasonal basis. To do this, four seasonal REI and SOI time series are formed by averaging three-month values. The four seasons consist of December-February (DJF), March-May (MAM), June-August (JJA), and September-November (SON). Then, all SOI values are categorized into five levels based on the magnitudes of individual data (Jin et al., 2005). The five categories of the SOI values are strong warm phase, weak warm phase, normal phase, weak cold phase, and strong cold phase. On the other hand, the seasonal REI data are converted into percentile ranked probability time series to remove periodicities in REI time series and to deal with the disparities among climate divisions. The percentile ranked probability values are based on Weibull plotting position formula. All REI values are ranked in ascending order and then divided by n + 1 (n: size of data).

Monthly REI composites on 24-month basis are computed for each climate division, starting with the July preceding the event, continuing through the June following the event year, for both high and low phases of the SO. The July preceding the event is designated as Jul (-), while the June following the event year is expressed as Jun (+). Composites are computed separately for each phase of the SO. The composite for each climate division is then fitted with the first harmonic of an idealized 24-month SO cycle (either warm or cold episodes). This method assumes one REI peak (or trough) during the duration of an SO event and that the SO is phase locked to the annual cycle. A 24-month compositing period was chosen since this defines the period during which one phase of the SO goes through its entire cycle (Rasmusson and Carpenter 1983). In the first harmonic cycle, the amplitude represents magnitude of the ENSO-related REI signals, and the angular phase indicates time of the peak anomaly from the mean value (Fig. 4). The formula of the harmonic fits are as follows (Wilks, 1995).

$$y_t = \bar{y} + \sum_{i=1}^{\frac{n}{2}} \left\{ C_i \cos\left[\frac{2\pi it}{N} - \beta_i\right] \right\}$$
$$= \bar{y} + \sum_{i=1}^{\frac{n}{2}} \left\{ A_i \cos\left[\frac{2\pi it}{n}\right] + B_i \sin\left[\frac{2\pi it}{n}\right] \right\}$$

$$A_i = \frac{2}{n}\sum_{t=1}^{n} y_t \cos\left(\frac{2\pi it}{n}\right), \quad B_i = \frac{2}{n}\sum_{t=1}^{n} y_t \sin\left(\frac{2\pi it}{n}\right), \quad C_i = \left(A_i^2 + B_i^2\right)^{0.5}$$

$$\beta_i = \tan^{-1}\frac{B_i}{A_i}\ (A_i > 0), \quad \frac{\pi}{2}\ (A_i = 0), \quad \tan^{-1}\frac{B_i}{A_i} \pm \pi\ (A_i < 0)$$

where y_t is monthly REI value, $\bar{y}$ is the mean REI value, t is time of observation, i is number of harmonic fits, n is sample size, C_i is amplitude of the harmonic curve (magnitude of curve), β_i is time of harmonic peak (temporal phase of curve), and A_i and B_i are Fourier coefficients.

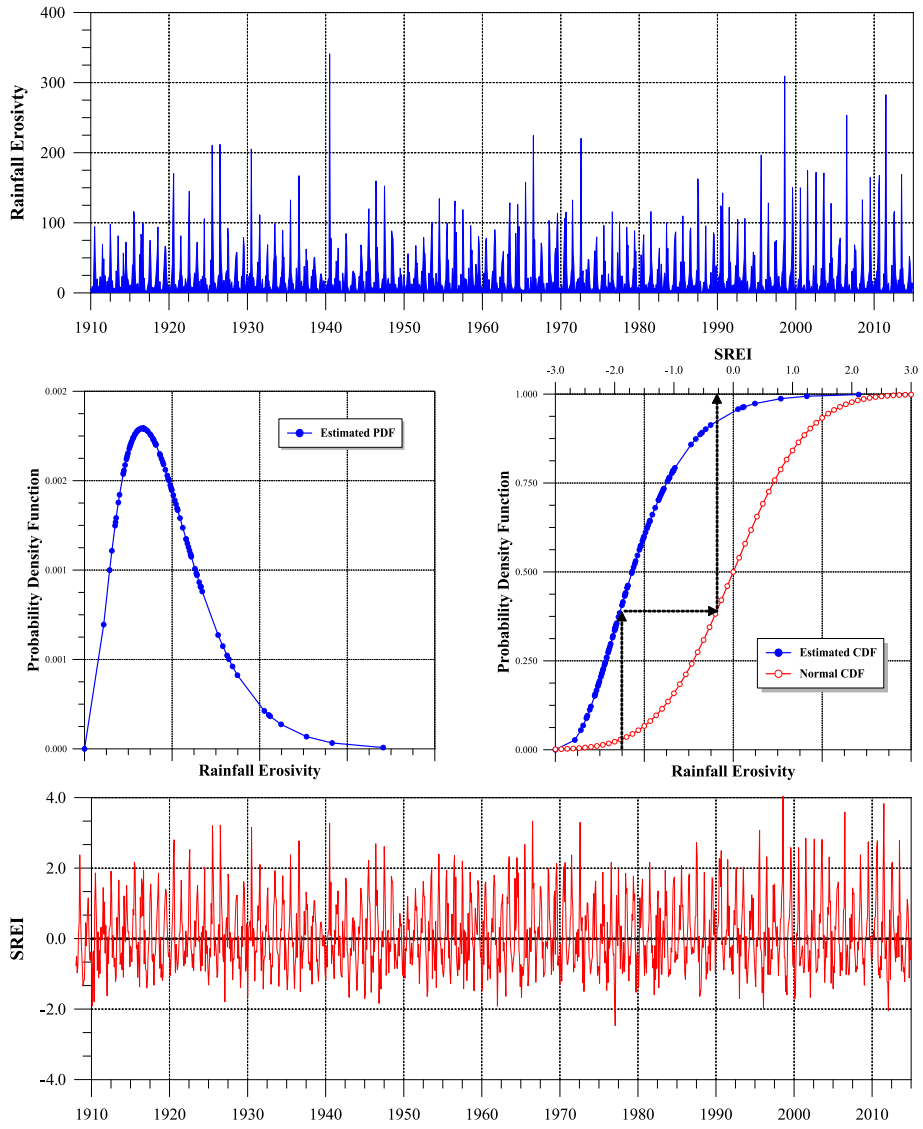

Fig. 3. SREI estimation procedure. Monthly REI data (upper) are fitted to a gamma distribution (middle left) and transformed into cumulative density function of standardized normal distribution by the equal-probability conversion technique (middle right) for calculating the standardized rainfall erosivity index (bottom).

After the climate division composites are fit with a 24-month harmonic, the amplitude and phase of the curve is plotted as a vector for each station. In the analysis convention chosen here the vector points toward the positive part of the cycle, that is, higher-than-normal rainfall erosivity. It is only after examining the composites, described below, that the actual sign of the SO-REI relationship can be determined. This study is concerned with regional areas of the United States that exhibit strong SO-REI relationships over periods of many months. Therefore, individual, or isolated, climate division that shows strong apparent relationships or areas that have short-time scale relationships are not considered for further study.

Plotting the harmonics as vectors on a map provides a method to spatially identify candidate geographic areas that appear to have a coherent ENSO response. We attempted to choose the largest areas of coherent ENSO response, where the "coherence" is estimated through the computation of the ratio of the magnitude of the average vector to the arithmetic average value of the vector magnitudes.

$$SC = \frac{\left[\left(\sum V\cos\theta\right)^2 + \left(\sum V\sin\theta\right)^2\right]^{1/2}}{\sum V}$$

where the numerator is the average vector magnitude of all harmonic vectors within the candidate regions, the denominator is the arithmetic average value of the vector magnitudes, θ is angle of the vector, and V is magnitude of the vector. The analysis that follows is limited to areas for which values of the coherence were equal to or greater than 0.80 (Ropelewski and Halpert, 1986). This eliminates from the analysis regions that contain harmonic vectors with large amplitudes at a few stations which have little consistency in phase, i.e., low coherence.

Aggregate composites are formed to detect the ENSO-related REI signal seasons. These signal seasons represent apparently consistent REI responses to the extreme ENSO forcing. All ENSO composite values in a candidate region are averaged and plotted on a 24-month period to cover the entire ENSO cycle and identify accurately the signal season. One season within the aggregate composite is found by detecting a group of values showing more than five consecutive months with the same sign. The event year and the following year are regarded as the responding period of ENSO phenomena, considering the distance between the study area in midlatitude and the ENSO area in the Pacific Ocean. Index Time Series (ITS) are computed by temporally averaging REI values of the signal seasons for the entire years of record and by spatially averaging the REI data over the candidate regions. The ITS values are used to quantify the temporal consistency of the ENSO impact on REI patterns. Temporal consistency rates for the candidate regions

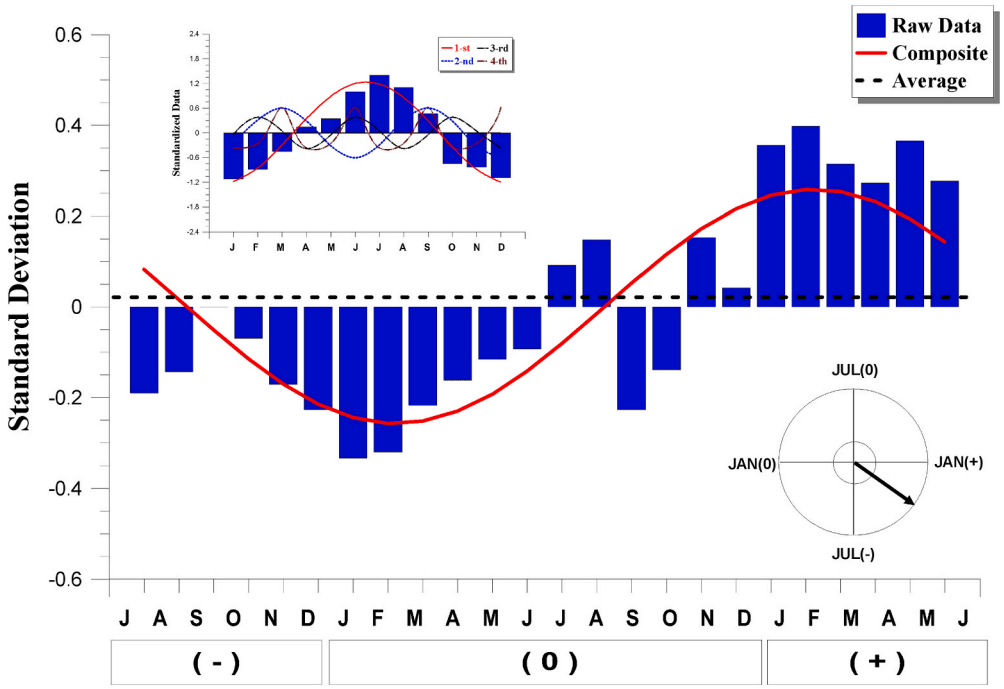

Fig. 4. A first harmonic fit to the rainfall erosivity ENSO composite for the climate division SC-5. The amplitude and the phase of the first harmonic are presented as a harmonic dial (the lower right). The inset diagram (the upper left) depicts an example illustrating several harmonic fits of annual cycle for monthly rainfall erosivity index (REI) from the first to the fourth harmonic.

are computed using the rate of the number of years exhibiting ENSO signal in ITS to the number of all ENSO event years. These temporal consistency rates are the determinant of the core regions showing consistent REI responses to ENSO phenomena. In addition, extreme REI events are examined in association with ENSO forcing as demonstrated by Ropelewski and Halpert (1986), Lee et al. (2020a,b). They investigated climate linkage between ENSO events and extreme precipitation occurrences. In the present study, the number of years showing the ENSO-related extreme REI signal is counted during the signal season. To assign the highest and lowest levels of the extreme events, the ITS time series are ranked from the highest value to the lowest value, normalized by the entire data, and transformed to the probability time series (Kahya and Dracup, 1994; Lee et al., 2018). The highest value is assigned to the probability of 80% ITS, while the lowest value is assigned to the probability of 20% ITS.

A machine learning technique, Gaussian Mixture Model (GMM), was employed for diminishing the degree of subjectivity when candidate regions were determined based on the magnitude and temporal phase of the ENSO-related REI signals. GMM algorithm is based on a statistical learning technique used in identifying a subset of discrete data which represent a feature space. As a measurable characteristic, the feature can describe phenomena being observed and the corresponding feature data can form a feature space by defining collectively the single or multidimensional range. For the purpose of classifying the candidate regions objectively, three features are selected in this study, i.e., the intensity of the ENSO-related REI teleconnection, temporal cycle of each REI response, and Köppen climate classification. All harmonic dial vectors fall somewhere in the feature space. The GMM method takes advantage of probability model instead of objective functions of distance measurements as opposed to the commonly used clustering techniques, e.g., fuzzy C-means or k-means, which are based on distance measures. In the GMM algorithm, each cluster is classified by a parametric probability density based on a mixture model of probability distribution followed by dataset, and the cluster structure is modeled by finite mixture. Although the GMM technique has been considered a powerful tool for cluster analysis in many research fields, there have been little attention to its practical application in hydro-climatological studies. The dimension of the input data affects largely the results of cluster analysis because the GMM is based on probability model. Therefore, it is of great importance to select appropriate feature subset for conducting cluster analysis. Multivariate distribution of a given dataset can be fitted with a normal mixture model for cluster structure. Multivariate data, y_n, which is composed of m independent samples with variables, comprises C clusters in the dataset, and a probability distribution is assigned to each sample with a density function. Mixture probability density function, pdf, is weighed for the densities of C clusters as follows.

$$pdf(y_n|\beta) = \sum_{i=1}^{C} p_i h_i(y_n|\mu_i, V_i)$$

where p_i is mixing proportions, h_i is normal probability density function, μ_i is mean of h_i, and V_i is variance matrix. If an indicator vector of y is $d = [d_1, \cdots, d_m]$ with $d_m = [d_{n1}, \cdots, d_{ni}]$, the mixture model log-likelihood is as follows.

$$L(\beta|y_1, \cdots, y_m, d_{ni}) = \sum_{n=1}^{N} ln\left[\sum_{i=1}^{C} d_{ni} p_i h_i(y_n|\mu_i, V_i)\right]$$

Also, the parameter $\beta = (p_1, \cdots, p_i, \mu_1, \cdots, \mu_i, V_1, \cdots, V_i)$ can be selected for maximizing the log-likelihood. Here, many normal mixture models can be chosen according to the geometric features of each cluster that includes the expression of the cluster variance matrix.

Hypergeometric distribution test is employed to assign the significance level of the ENSO-REI correlation. Haan (1977) conducted the hypergeometric distribution test calculating "the cumulative probability that at least m successes are obtained in n trials from a finite population of size N containing k successes". A cumulative probability computed from the hypergeometric distribution gives an occurrence significance level of the relationship previously defined for both extreme phases of the ENSO. Kahya and Dracup (1994) used hypergeometric test in terms of average value and high-low extreme events. In the present test, two cases (I and II) are considered according to the definition of a success. In case I, a success is defined as the occurrence of year that an ITS value

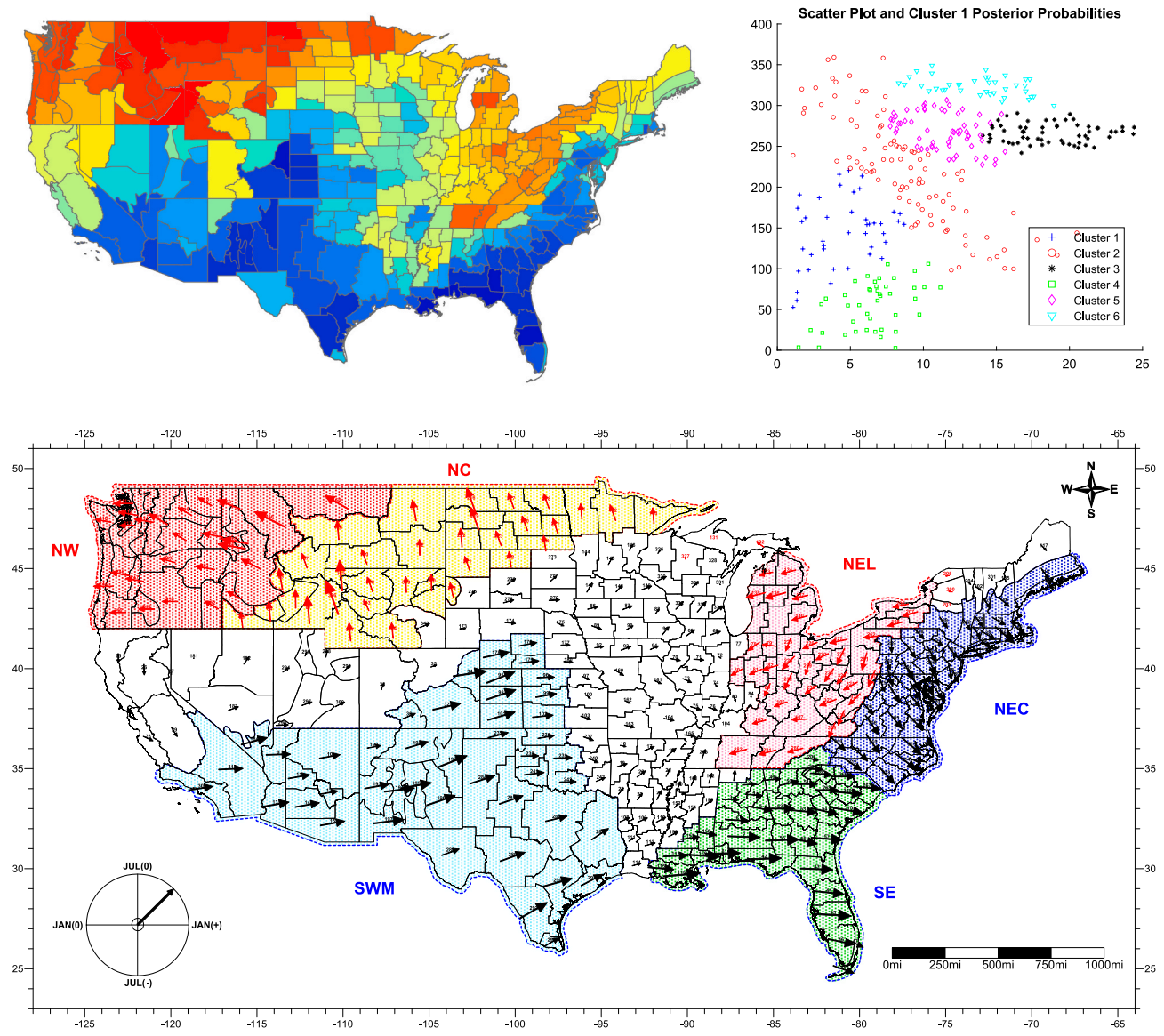

Fig. 5. Image map (upper left), clustering results (upper right) and harmonic dial map (lower) based on the first harmonic of the 2-year El Niño composites. Scale for the direction of arrows: south, July(−); west, January(0); north, July(0); and east, January(+). The magnitude of arrows is proportional with the amplitude of the harmonics.

associated with ENSO events is higher (lower) than the median, while in case II, a success is defined as the occurrence of year in which an ITS value associated with ENSO events falls into the upper (lower) 20% of the distribution. Annual cycle analysis is used as a comparative interpretation of two ENSO effects on the REI anomaly from the perspective of magnitude and annual trend of the signal. Monthly REI time series are transformed into modular coefficients for carrying out annual cycle analysis. These modular coefficients remove the effects of dispersed variance and mean values. The REI data are expressed as percentages for the annual mean values. The modular coefficient data are calculated by the rate of each monthly REI value to the monthly average value for the entire data. This annual cycle plots make it possible to determine whether the extreme phases of warm and cold ENSO events modulate REI increasingly or decreasingly. Cross-correlation coefficients are calculated on a seasonal basis to compare the positive and negative ENSO-related REI signals. Five categorized SOI data sets as ENSO index are correlated with the monthly REI time series expressed by percentile ranked probability. The resulting correlation coefficient values indicate the magnitude and sign of the relationship between the REI patterns and the ENSO forcing on a seasonal basis. More detailed explanation of the

Table 2
Properties of the candidate regions (El Niño events).

Region	Season	Coherence	Total Episode	Occurrence Episode	Consistency	Extreme Events
NW	Sep (0) – May (+)	0.93	29	23	79 %	9
NC	Nov (0) – Apr (+)	0.95	29	21	72 %	10
NEC	Nov(0) – May (+)	0.98	29	18	62 %	11
SE	Sep (0) – Mar (+)	0.98	29	22	76 %	12
SWM	Sep (0) – Apr (+)	0.98	29	25	86 %	14

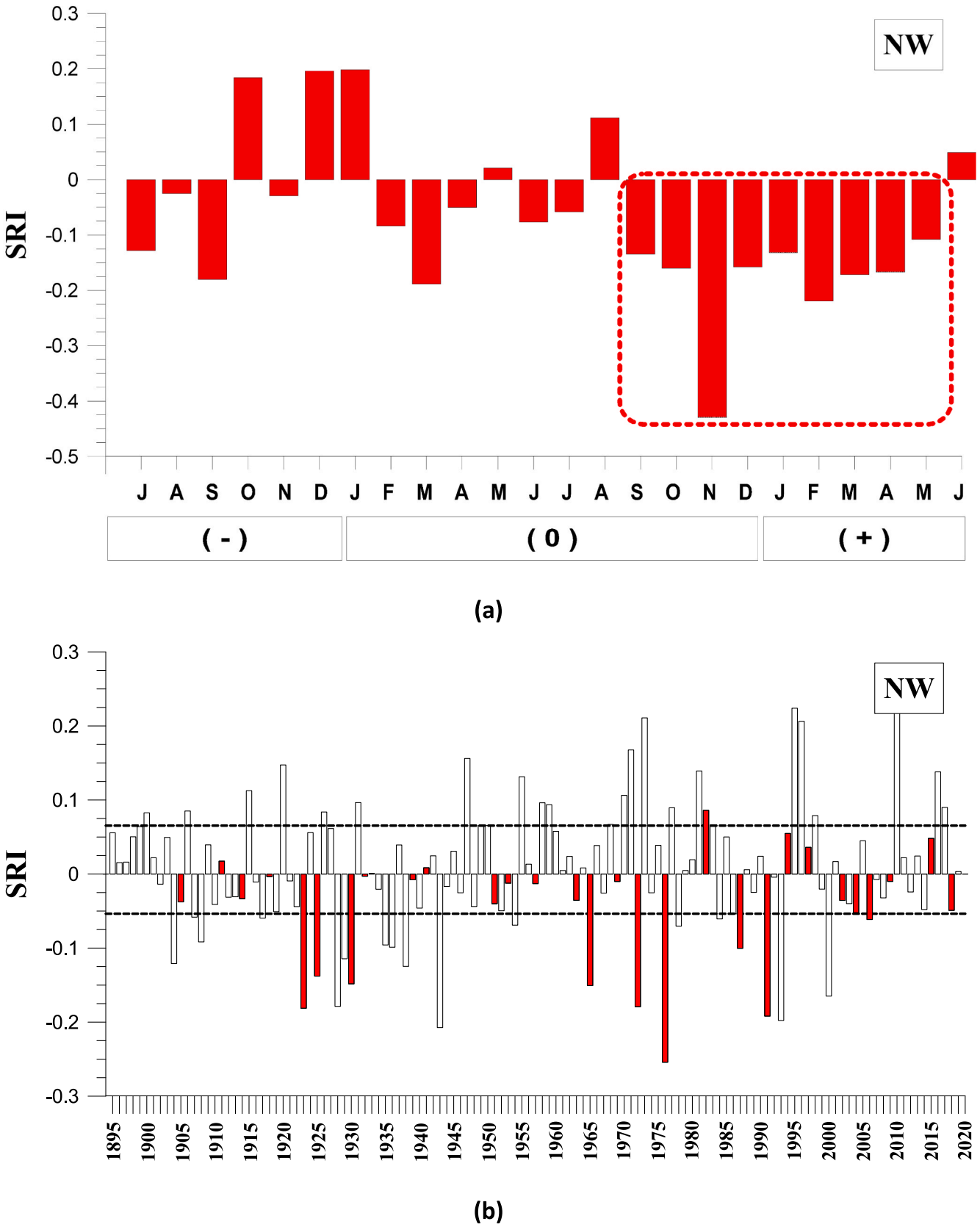

Fig. 6. (a) El Niño aggregate composite for the candidate NW region. The dashed line box delineates the season of possible El Niño-related responses. (b) The index time series for the NW region for the season previously detected. El Niño years are shown by solid bars. The dashed horizontal lines are the upper (80%) and lower (20%) limits for the distribution of ITS values.

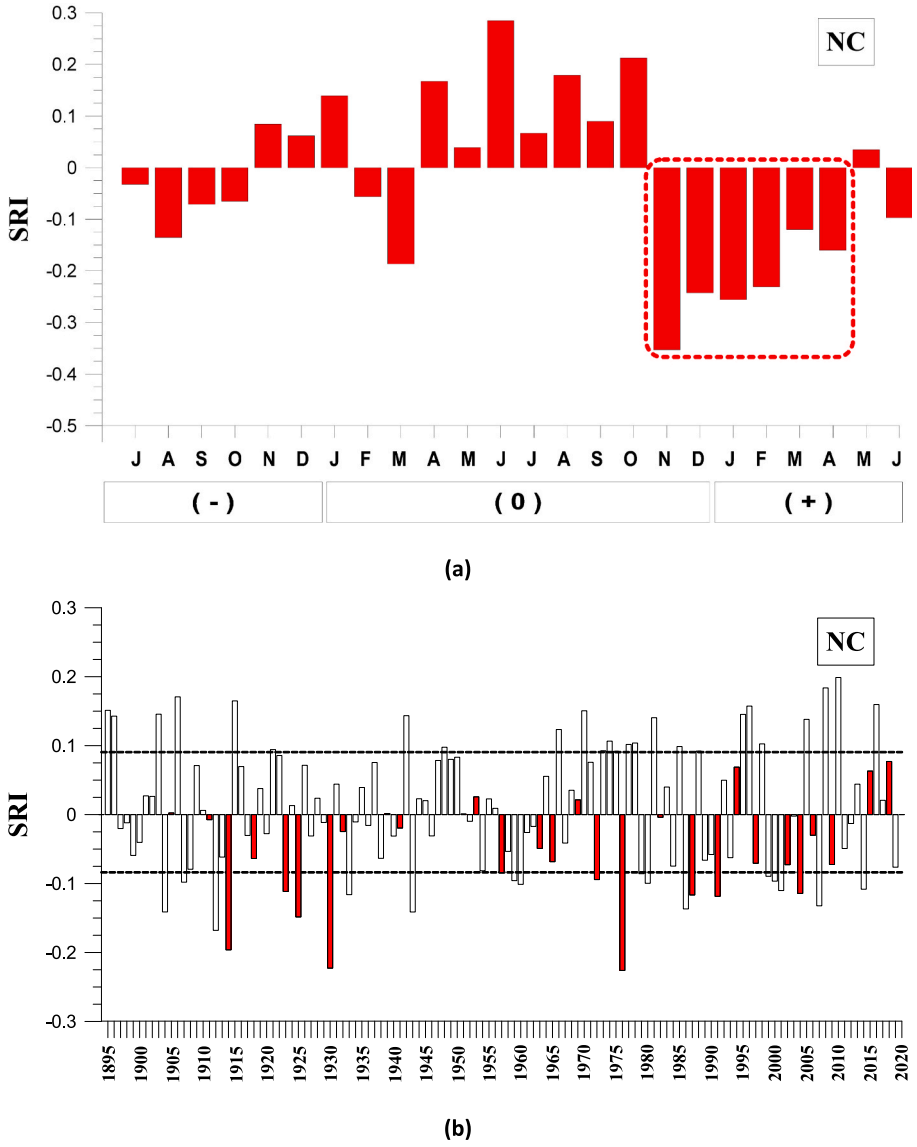

Fig. 7. As in Fig. 6, except for the candidate NC region.

data conversion and correlation procedure was described in the first section of data processing.

4. Results

4.1. El Niño-rainfall erosivity relationship

Fig. 5 shows the harmonic dial map with the detected candidate regions from the results of composite and harmonic analyses. The vectorial map for REI indicates six regions of the United States that appear to have ENSO-related signals. The candidate regions are the northwest (NW), the north central (NC), the northeast inland (NEL), the northeast coastal (NEC), the southeast (SE), and the southwest/middle-inland (SWM) regions. As shown in Table 2, composite rainfall erosivity indices for each region indicate that the NW, NC, NEC, SE, and SWM regions have an ENSO-related response. The REI composites for the five candidate regions show clearly defined positive and negative signal seasons within the ENSO cycle and thus they are explained in detail for further consideration in this analysis. However, the composite for the NEL region shows no significant signals within the ENSO cycle and thus this region is eliminated from further consideration.

The North-West region (NW) includes 26 climate divisions, extending from Washington and northern Oregon to western Montana and northern Wyoming, and including almost all of Idaho. The time series of the September (0) to May (+) REI indices averaged over all climate divisions in the NW region (Fig. 6) illustrates the notable consistency in the rainfall erosivity with respect to the ENSO in this part of the United States. This season showed below normal, i.e., lower than the average REI for 23 out of 29 ENSO events. Further, of the 25 occurrences of index values equal to or lower than the lowest ITS limit (20%), 9 of them occurred in association with ENSO. One of the occurrences in the highest ITS limit (80%) was associated with ENSO. The spatial coherence and temporal consistency were 0.93 and 0.79.

The North Central region (NC) occupies all of North Dakota, the southern part of South Dakota, the northern part of Minnesota, parts of Idaho and Montana, and almost all of Wyoming. REI time series of the NC region based on the climate division data for the November (0) to April (+) season (Fig. 7) shows below normal REI for 21 out of the 29 ENSO events. While the index shows values of lower than or equal to the lowest ITS limit (20%) for 10 of the ENSO years, negative values of the same magnitude or lower also occur during 13 non-ENSO-related years. None of the ENSO-related seasons in the NC area falls into the highest ITS limit (80%). The spatial coherence and temporal consistency were 0.95 and 0.72.

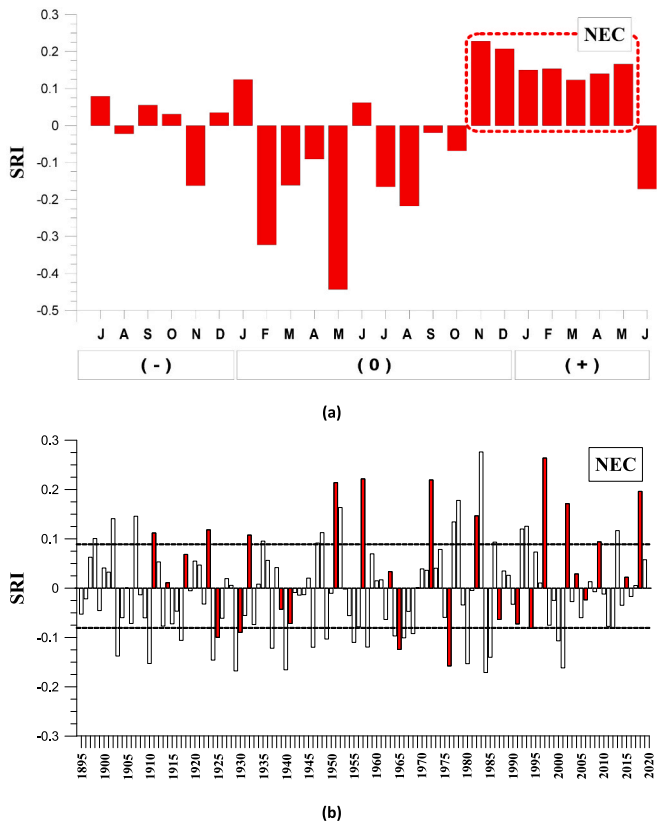

Fig. 8. As in Fig. 6, except for the candidate NEC region.

The Northeast Coastal region (NEC) has the smallest area but contains the largest number of climate divisions among all candidate regions. The NEC regions contains 47 climate divisions and covers almost all of North Carolina and Virginia, eastern Pennsylvania and New York, and all of Maryland, Delaware, New Jersey, Connecticut, Massachusetts, Rhode Island. REI time series of the NEC region based on the climate division data for the November (0) to May (+) season (Fig. 8) shows above normal REI for 18 out of the 29 ENSO events. While the index shows values of greater than or equal to the highest ITS limit (80%) for 11 of the ENSO years, positive values of the same magnitude or greater also occur during 12 non-ENSO-related years. Only two of the ENSO-related seasons in the NEC area fall into the lowest ITS limit (20%). The spatial coherence and temporal consistency were 0.98 and 0.62.

The Southeast region (SE) covers 37 climate divisions, and includes all of Florida, Georgia, South Carolina, parts of Louisiana and Mississippi, and almost all of Alabama. The time series of the September (0) to March (+) REI indices averaged over all stations in the SE region (Fig. 9) illustrates the notable consistency in the REI with respect to the ENSO in this part of the United States. This season showed above normal, i.e., greater than the average REI for 22 out of 29 ENSO events. Further, of the 25 occurrences of index values equal to or greater than the highest ITS limit (80%), 12 of them occurred in association with ENSO. Only one of the occurrences in the lowest ITS limit (20%) was associated with ENSO. The spatial coherence and temporal consistency were 0.98 and 0.76.

The Southwest/Middle-Inland region (SWM) consists of southern California, eastern Colorado, western Kansas and Oklahoma, part of Nevada and Nebraska, and all of Arizona, New Mexico and Texas, and covers 46 climate divisions. Time series of the rainfall erosivity for the SWM region, September (0) to March (+) in Fig. 10, shows another example of conclusive result. 25 out of 29 ENSO seasons are associated with above median REI in the time series based on the climate division data. Since the probability of getting 25 observations of the same sign strictly by chance is relatively low, the result is statistically significant. The REI index exceeded the 80% index value with 14 ENSO episodes, and only one of the occurrences in the lowest ITS limit (20%) was associated with ENSO. The spatial coherence and temporal consistency were 0.98 and 0.86. Thus, it appears that ENSO is a reliable discriminator of the REI anomalies of the SWM region.

4.2. *La Niña-rainfall erosivity relationship*

For 22 La Niña episodes, which is the cold phase of ENSO, the composite and harmonic analyses were performed on the monthly REI data. The resulting map of harmonic dial vectors (Fig. 11) indicates notable responses within the six outlined regions, the northwest (NW), the north central (NC), the northeast inland (NEL), the northeast coastal (NEC), the southeast (SE), and the southwest/middle-inland (SWM) regions. ENSO composites of REI indices for each of the regions (Figs. 12-16) indicate that the five regions have well-defined seasons of potentially significant ENSO-related response except for the NEL region. The composite for the NEL region shows no significant signals within the ENSO cycle and thus this region is eliminated from further consideration. The overall results of the composite and harmonic analyses are outlined in Table 3.

The Northwest region (NW) occupies all of Washington, Oregon, Idaho, Montana, and the northwestern part of Wyoming, and covers 37 climate divisions. Time series of the standardized REI departure averaged over the all climate divisions in the NW region for the October (0) to February (+) season (Fig. 12) shows positive REI departure for 17 out of 22 ENSO events. The index values equal or exceed the highest ITS limit (80%) in 12 of the ENSO years. Only two of the occurrences in the lowest limit (20%) was associated with ENSO. The spatial coherence and temporal consistency were 0.96 and 0.77.

The North Central region (NC) includes 22 climate divisions, extending from North Dakoda to northern Michigan, and including part of South Dakoda and almost all of Minnesota. In the NC region the apparent ENSO-related REI response occurs in August (0) to February (+). The time series of spatially averaged standardized REI departures for this season (Fig. 13) shows positive departures for 16 out of 22 ENSO events. The index shows values of higher than or equal to the highest ITS limit (80%) for 6 of the ENSO years. Only two of the ENSO-related seasons in the NC area fall into the lowest ITS limit (20%). The spatial coherence and temporal consistency were 0.94 and 0.73.

The Northeast Coastal region (NEC) has the smallest area, contains 47 climate divisions, and covers almost all of West Virginia and Pennsylvania, eastern North Carolina, and all of Maryland, Delaware, New Jersey, Massachusetts, and Virginia. In the NEC region the apparent ENSO-related REI response occurs in November (0) to May (+). The time series of spatially averaged standardized REI departures for this season (Fig. 14) shows negative departures for 17 out of 22 ENSO events. The index shows values of lower than or equal to the lowest ITS limit (20%) for 8 of the ENSO years. None of the ENSO-related seasons in the NEC area fall into the highest ITS limit (80%). The spatial coherence and temporal consistency were 0.94 and 0.77.

The Southeast region (SE) consists of eastern North Carolina and all of South Carolina, Georgia, Alabama, Florida, and covers 34 climate divisions. Time series of the standardized REI departure averaged over the all climate divisions in the SE region for the November (0) to May (+) season (Fig. 15) shows negative REI departure for 18 out of 22 ENSO events. The index values equal or exceed the lowest ITS limit (20%) in 8 of the ENSO years. None of the occurrences in the highest limit (80%) was associated with ENSO. The spatial coherence and temporal consistency were 0.97 and 0.77.

The Southwest/Middle-Inland region (SWM) covers 56 climate divisions, and includes all of Arizona, New Mexico, Texas, and Oklahoma, almost all of Nebraska and Kansas, eastern Colorado, and southern California, Nevada, and Utah. In the SWM region, the notable ENSO-related REI response occurs in roughly the same season October (0) to

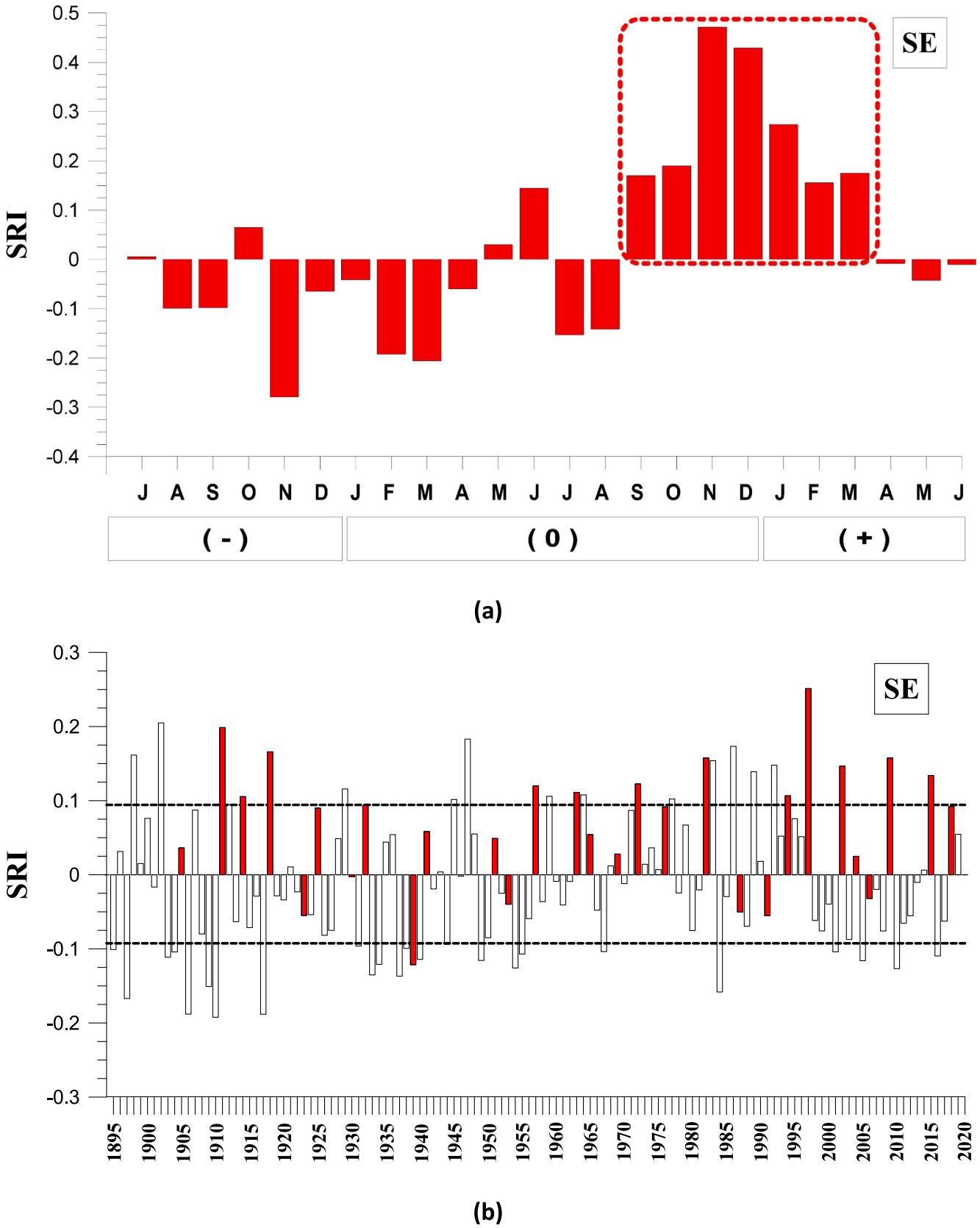

Fig. 9. As in Fig. 6, except for the candidate SE region.

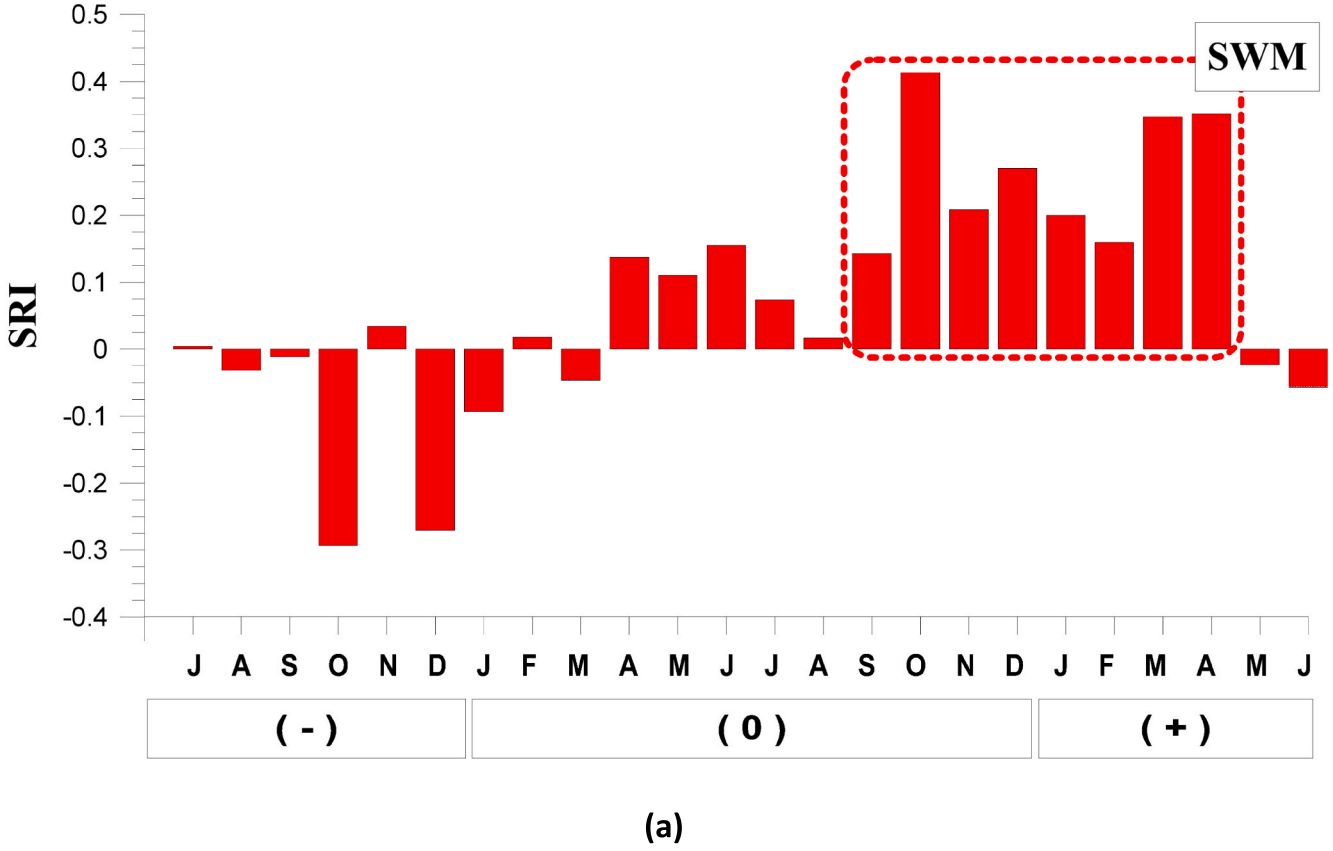

(a)

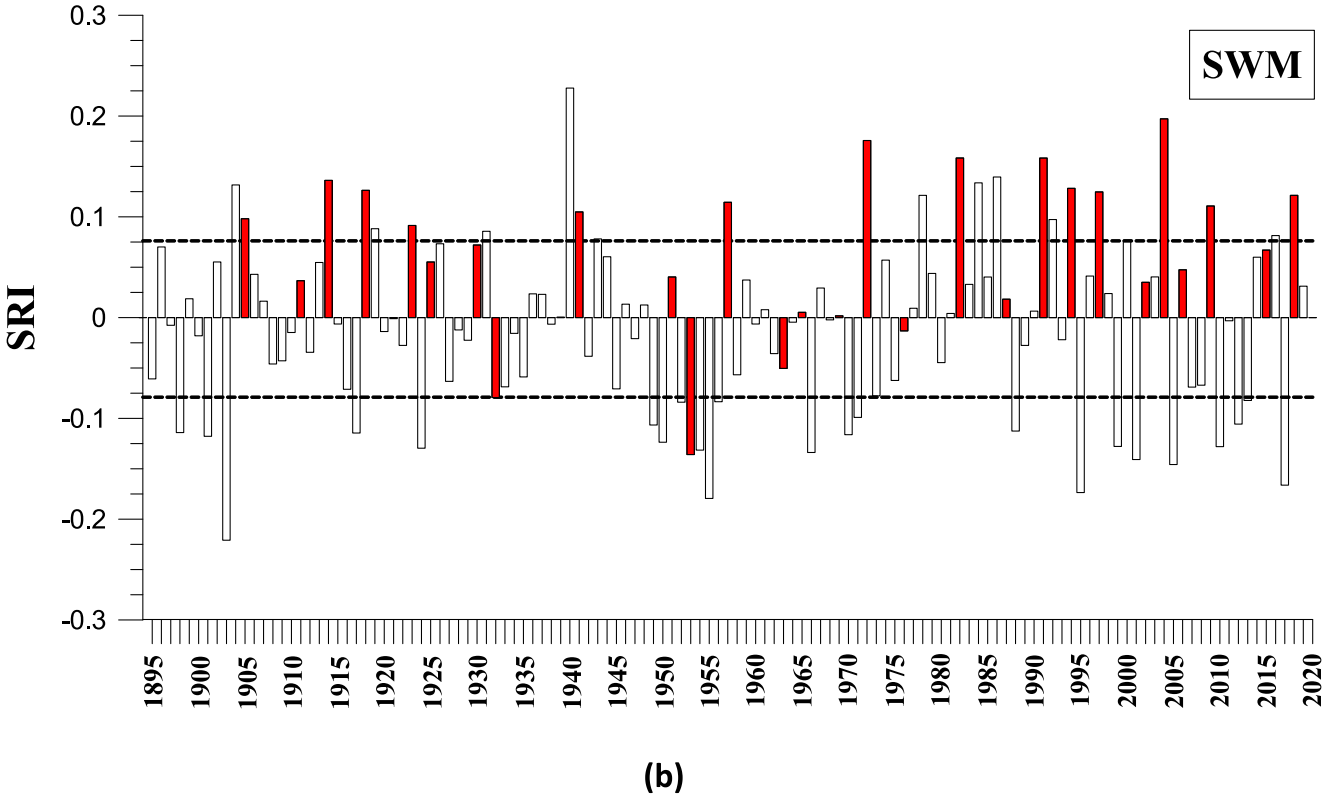

(b)

Fig. 10. As in Fig. 6, except for the candidate SWM region.

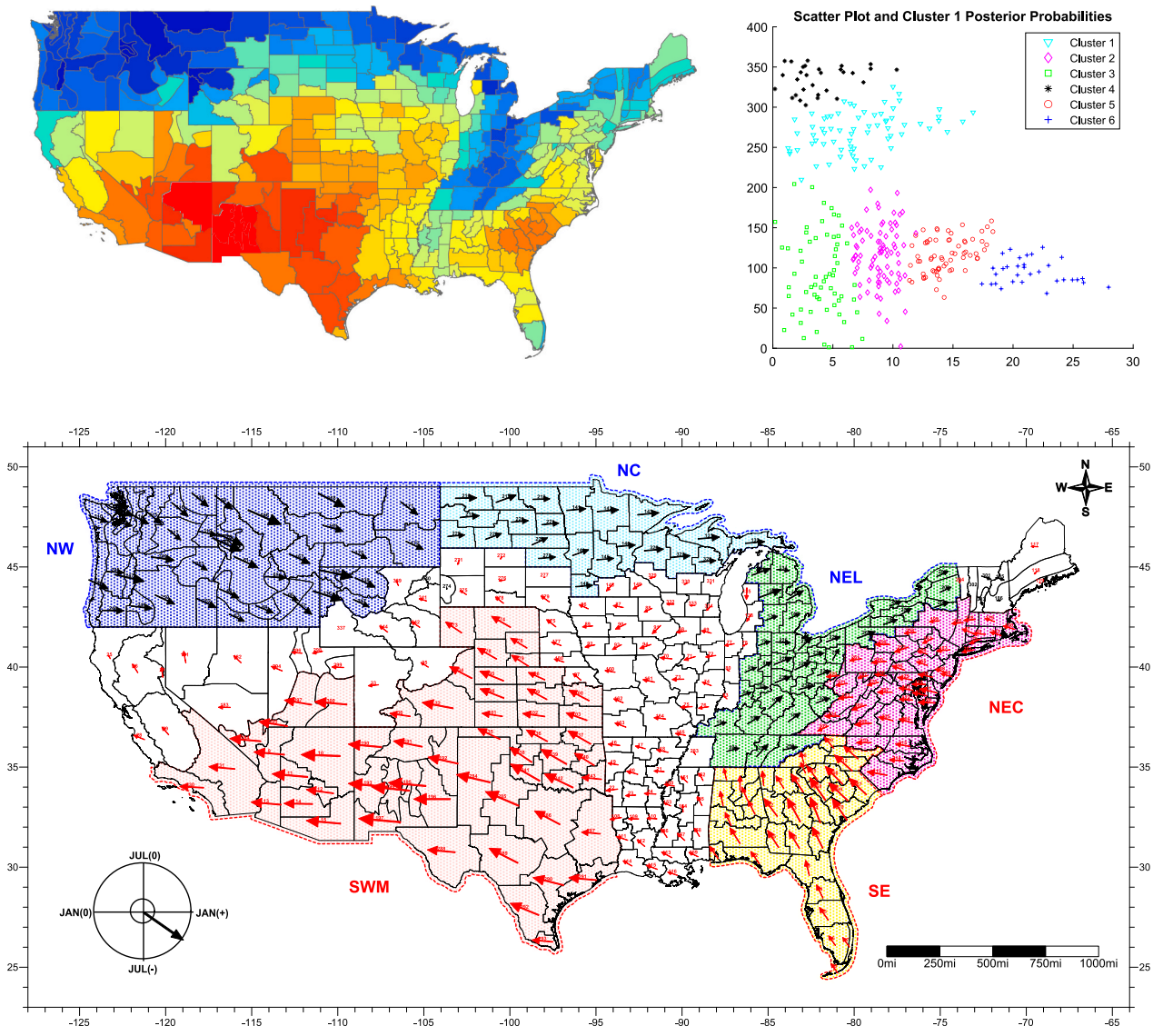

Fig. 11. As in Fig. 5, except for La Niña composites.

June (+) in Fig. 16, as the REI response in SE region. 17 out of 22 ENSO seasons are associated with below median REI in the time series based on the climate division data. Moreover, of the 25 occurrences of index values equal to or smaller than the lowest ITS limit (20%), 9 of them occurred in association with ENSO. Only two of the occurrences in the highest ITS limit (80%) was associated with ENSO. The spatial coherence and temporal consistency were 0.95 and 0.77.

4.3. Comparative analysis of El Niño and La Niña

The probability that positive (negative) signal season occurs at random during the ENSO event years was tested by the hypergeometric distribution. In case I, the application of the hypergeometric distribution model results in a very low level of probability of occurrence by chance (less than 0.027) for both events. In case II, the probability is also very low for both phases of extreme events except for the NC region for the La Niña events. The extreme high REI conditions appear to be almost exclusively related to ENSO events in the 125-yr period. Overall results in Tables 4 and 5 are also consistent with the high confirmation rates (62–86% for El Niño events and 73–82% for La Niña events) for temporal consistency of the signals. All of this implies that the relationship depicted in the aggregate composites is probably due to nonrandom forcing mechanism, i.e., the tropical thermal anomalies.

Monthly REI time series are transformed into modular coefficients for carrying out annual cycle analysis. From this resulting series, El Niño and La Niña composites are formed and plotted along with the regional annual cycle (Figs. 17 and 18). Examination of this figures reveals two fundamental features. First, for a typical REI behavior during El Niño events, a suppressed REI of the annual cycle during the event year is followed by an enhanced REI of the annual cycle from the end of event year to the beginning of the following year. Second, for typical REI behavior during La Niña events, a somewhat increased amplitude during the event year precedes a decreased amplitude from the end of the event year to the beginning of the following year. This enhancement and suppression of magnitudes are roughly concurrent with the previously detected positive and negative signal seasons in five core regions. Also, an opposite tendency in monthly REI fluctuations between the El Niño and the La Niña composites during 24-month period are noticeable. In summary, the resulting findings suggest that the tropical heating (cooling) anomalies modulate the annual REI cycle within the United States by increasing (decreasing).

Table 6 displays the results of calculating cross-correlation coefficients. These values represent intensity and sign of the correlation between the ENSO phenomena and REI anomalies. This correlation

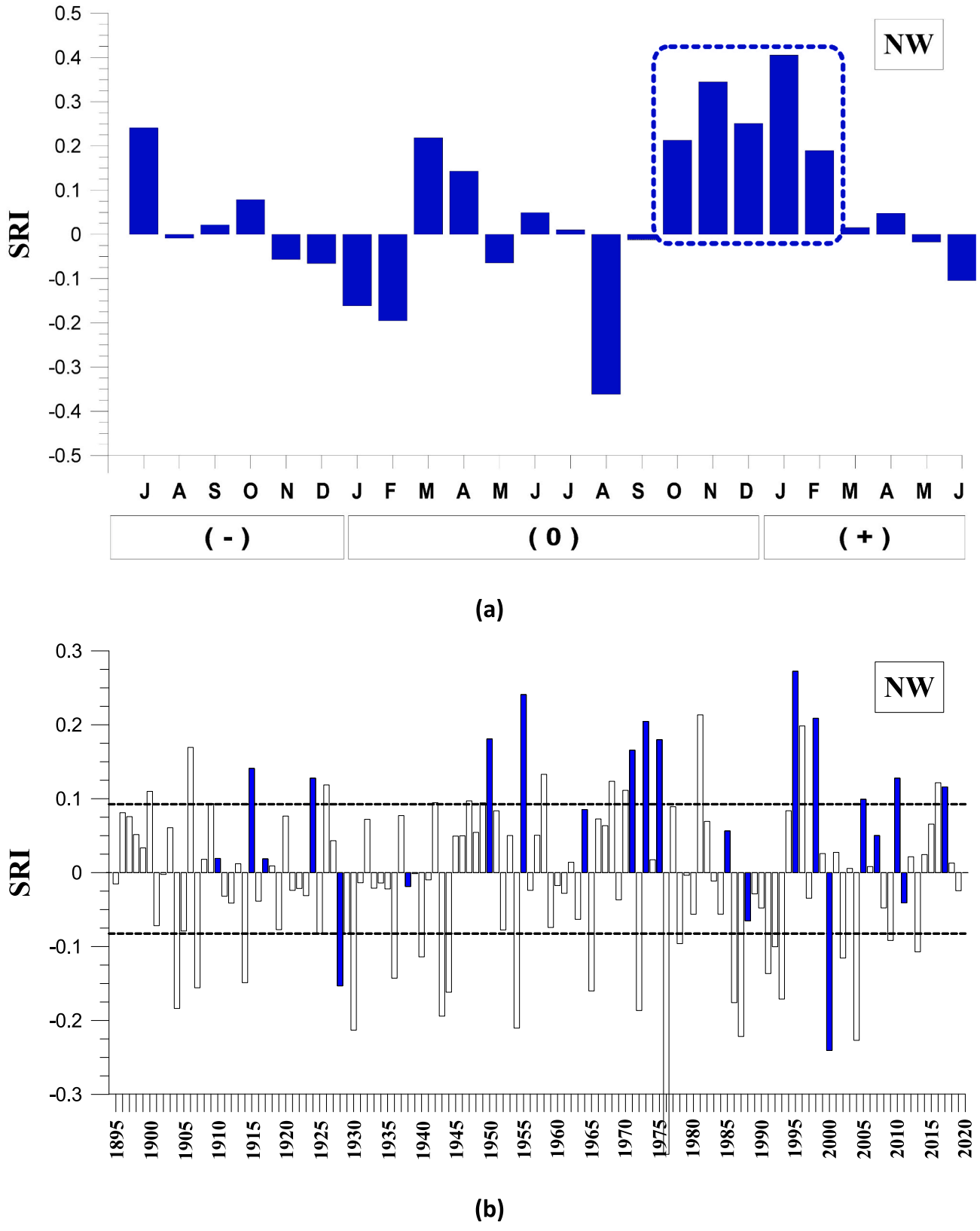

Fig. 12. (a) La Niña aggregate composite for the candidate NW region. The dashed line box delineates the season of possible La Niña-related responses. (b) The index time series for the NW region for the season previously detected. La Niña years are shown by solid bars. The dashed horizontal lines are the upper (80%) and lower (20%) limits for the distribution of ITS values.

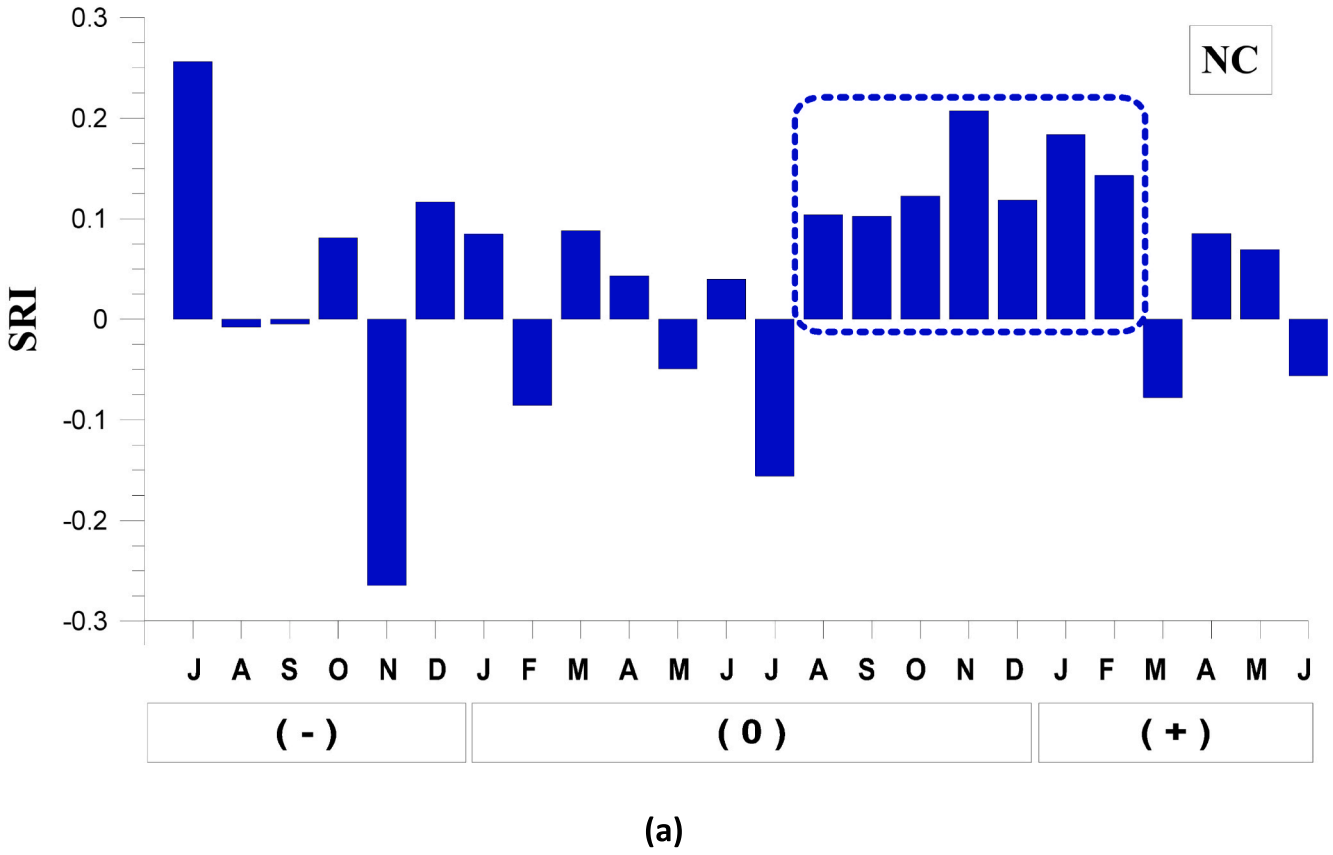

(a)

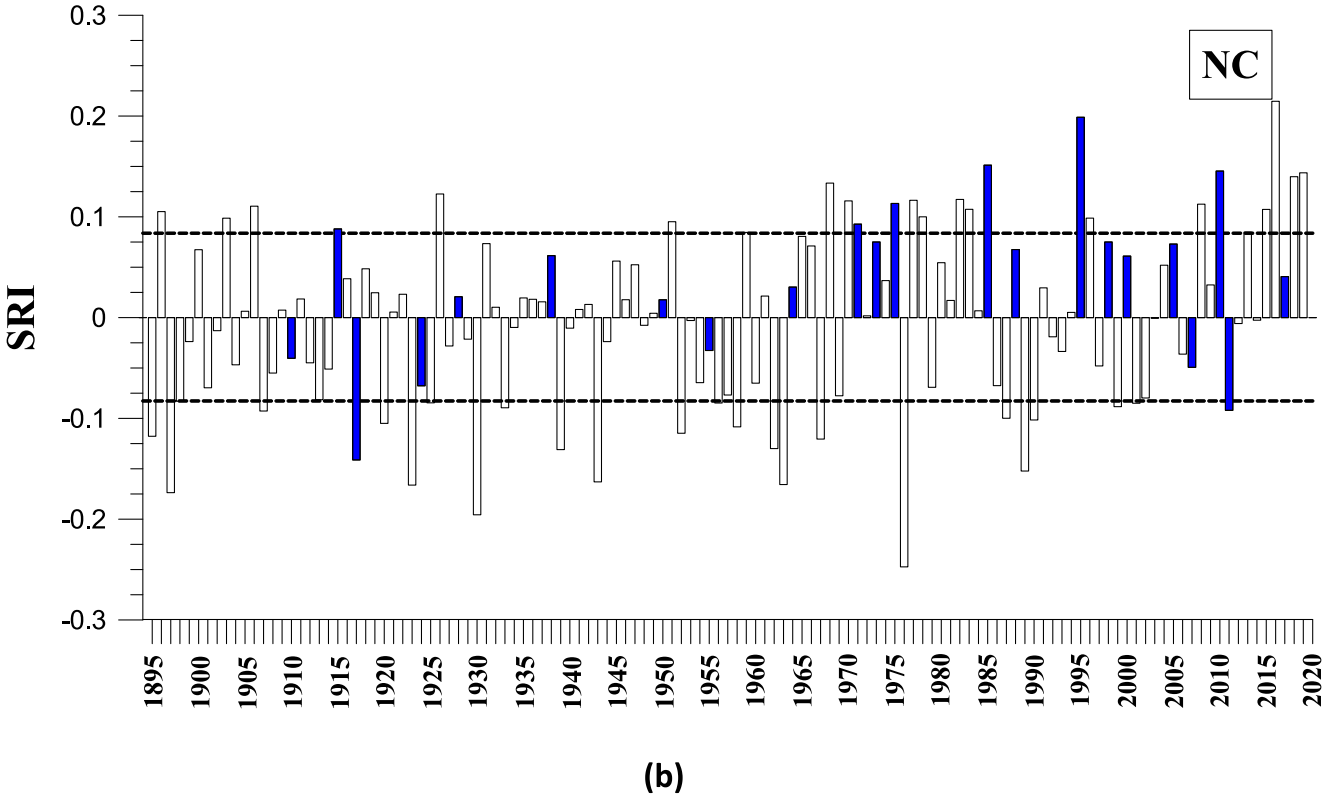

(b)

Fig. 13. As in Fig. 12, except for the candidate NC region.

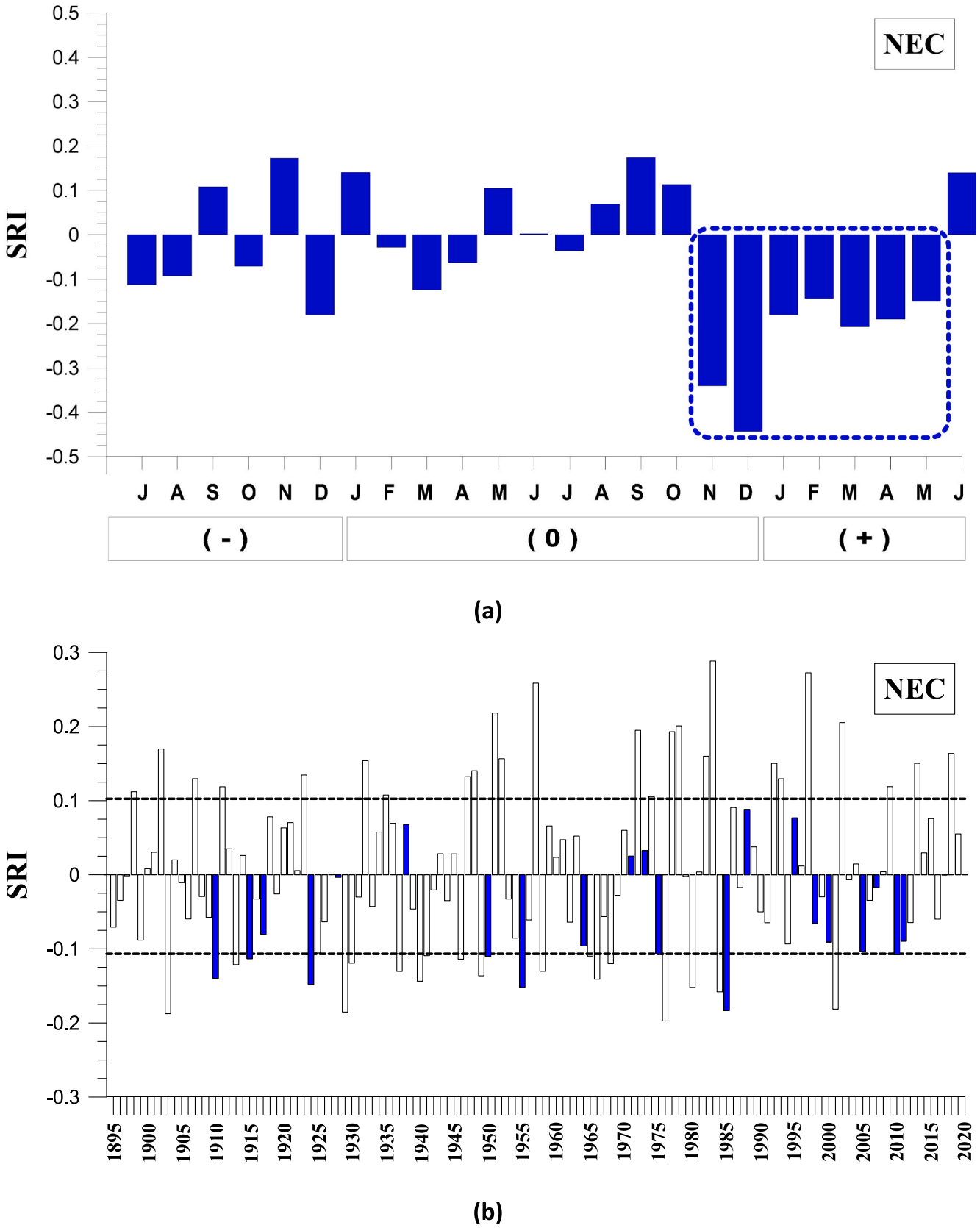

Fig. 14. As in Fig. 12, except for the candidate NEC region.

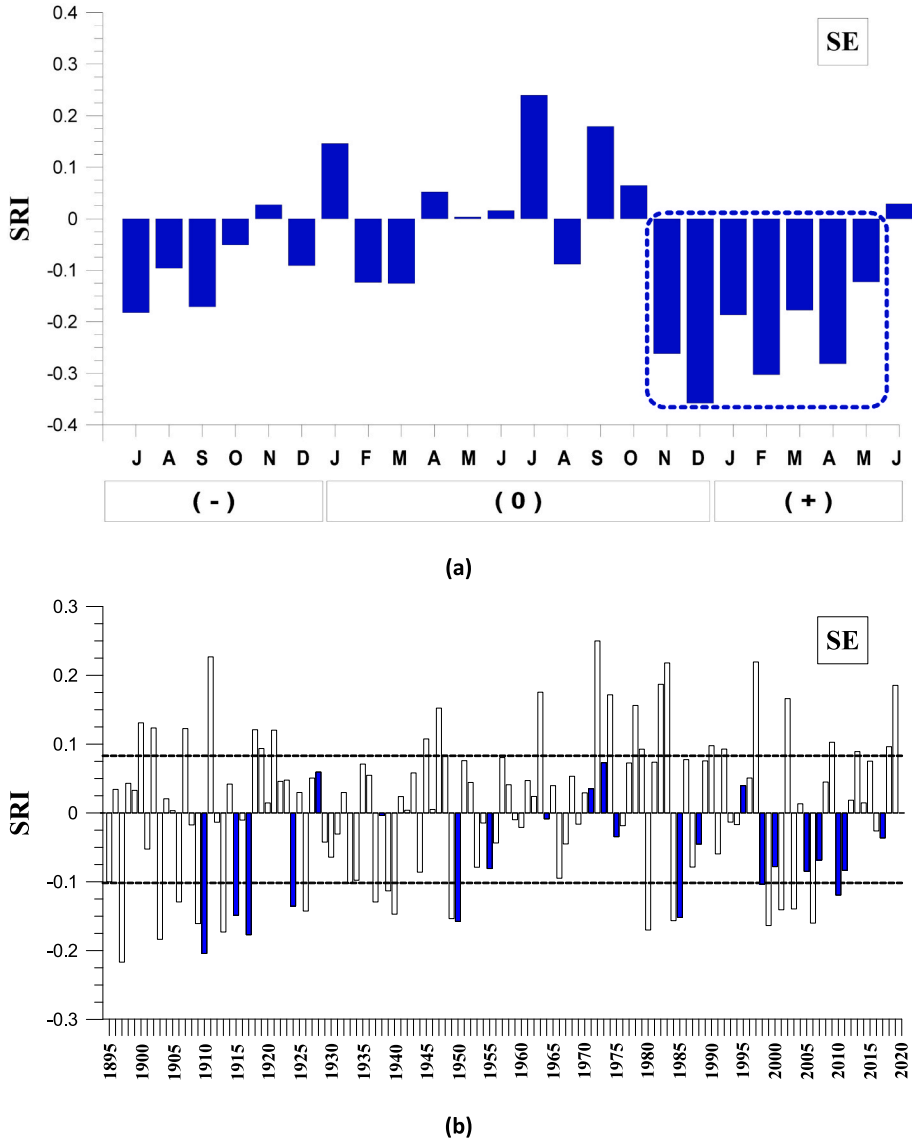

Fig. 15. As in Fig. 12, except for the candidate SE region.

analysis is conducted for large-scale climate indicator (ENSO index) and the seasonal REI anomalies, which use five categorized SOI data sets and percentile ranked probabilities, respectively. As a result, the seasonal REI anomalies were significantly correlated with both extreme phases of SO at 0.05 significance level. The highest positive correlation coefficient values are shown in the lag-2 to lag-3 cases over the NW region, and negative correlations are found in the lag-1 to lag-3 cases over the NEC and SE regions for the strong warm phase SOI condition. For the strong cold phase SOI condition, the highest negative correlation coefficient values are found at the NW region with lag-2 to lag-3 cases, and positive correlations are shown at the NEC and SE regions with lag-2 to lag-3 cases. The strong warm phase SOI provides prediction information of REI anomalies over NW (NEC and SE) region two to three (one to three) seasons in advance, while the strong cold phase SOI can be a predictor of REI anomalies over NW, NEC, and SE regions two to three seasons in advance. As a result, the stronger warm and cold phases of ENSO forcing, the more and less REI with lag time 1 to 3 seasons over the United States.

5. Discussions

As shown in Figs. 5 to 10, the results of this study show negative (positive) REI response to the El Niño events at the NW and NC regions (NEC, SE, and SWM regions) during fall (0) to spring (+) seasons. Especially, amplitude of the positive REI departure of El Niño year at the SE region is even higher than that of non-El Niño year. On the contrary, during the cold phase of ENSO phenomena, the opposite patterns are detected (Figs. 11 to 16). The monthly REI indices are higher (lower) than normal for the NW and NC (NEC, SE, and SWM) core regions from fall (0) through spring (+) seasons. The amplitude of the negative REI departure of the La Niña year at the SWM region is much higher than that of non-event year.

The opposite pattern of climate anomalies over the western parts of the United State (between the NW region and the SWM region) was documented in earlier studies (Cayan and Webb, 1992; Emery and Hamilton, 1985; Cayan and Peterson, 1989) and was consistently shown in the relevant composites of the extreme phase of ENSO forcing. Cayan and Webb (1992) stated that during the mature warm phase of ENSO phenomena in association with deepening of the Aleutian Island low pressure the northward shift of the North Pacific storm paths causes wet conditions over Alaska and western Canada and dry conditions over the northwestern US. On the other hand, the study by Emery and Hamilton (1985) showed that during the La Niña events the depression of the Central Pacific low, which is located over the Aleutian and Gulf of

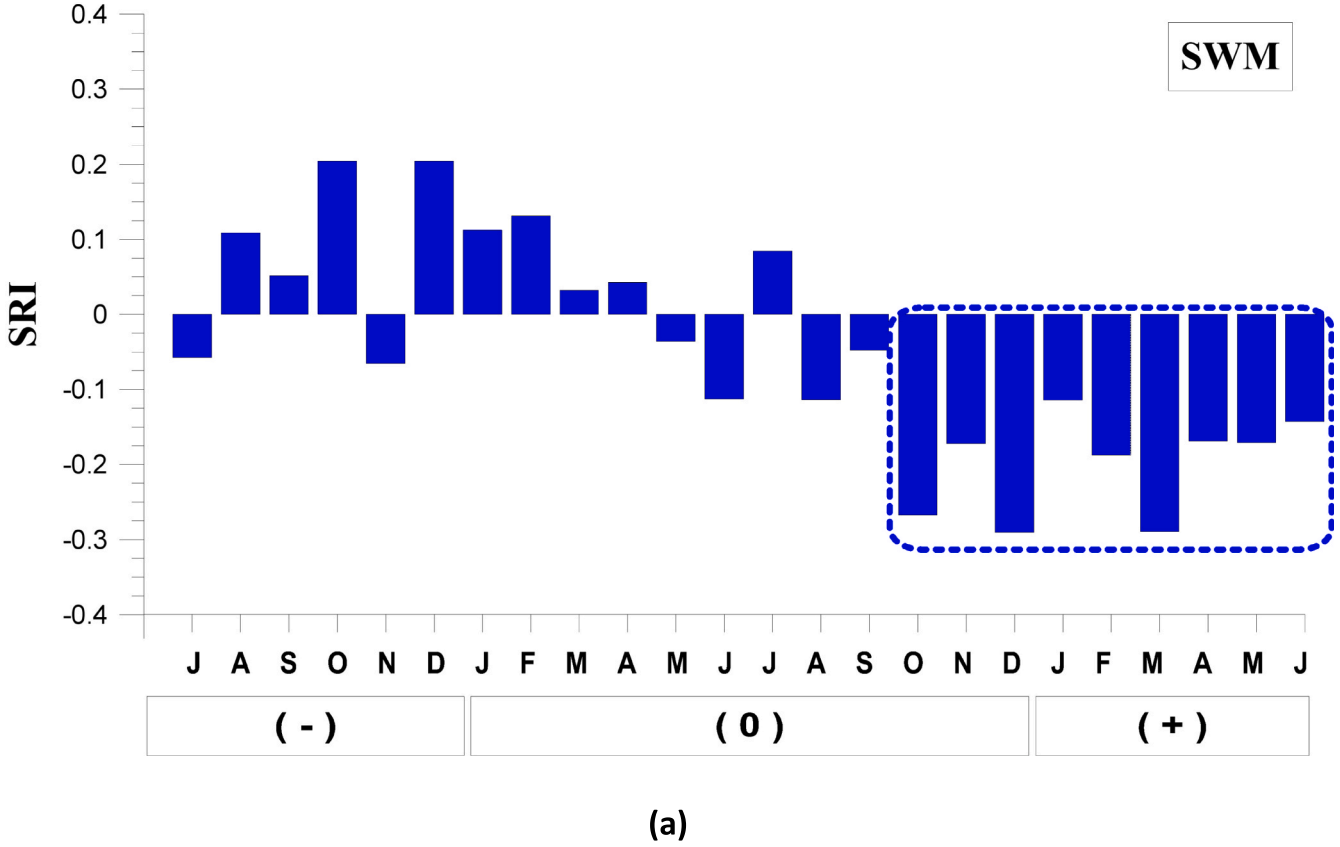

(a)

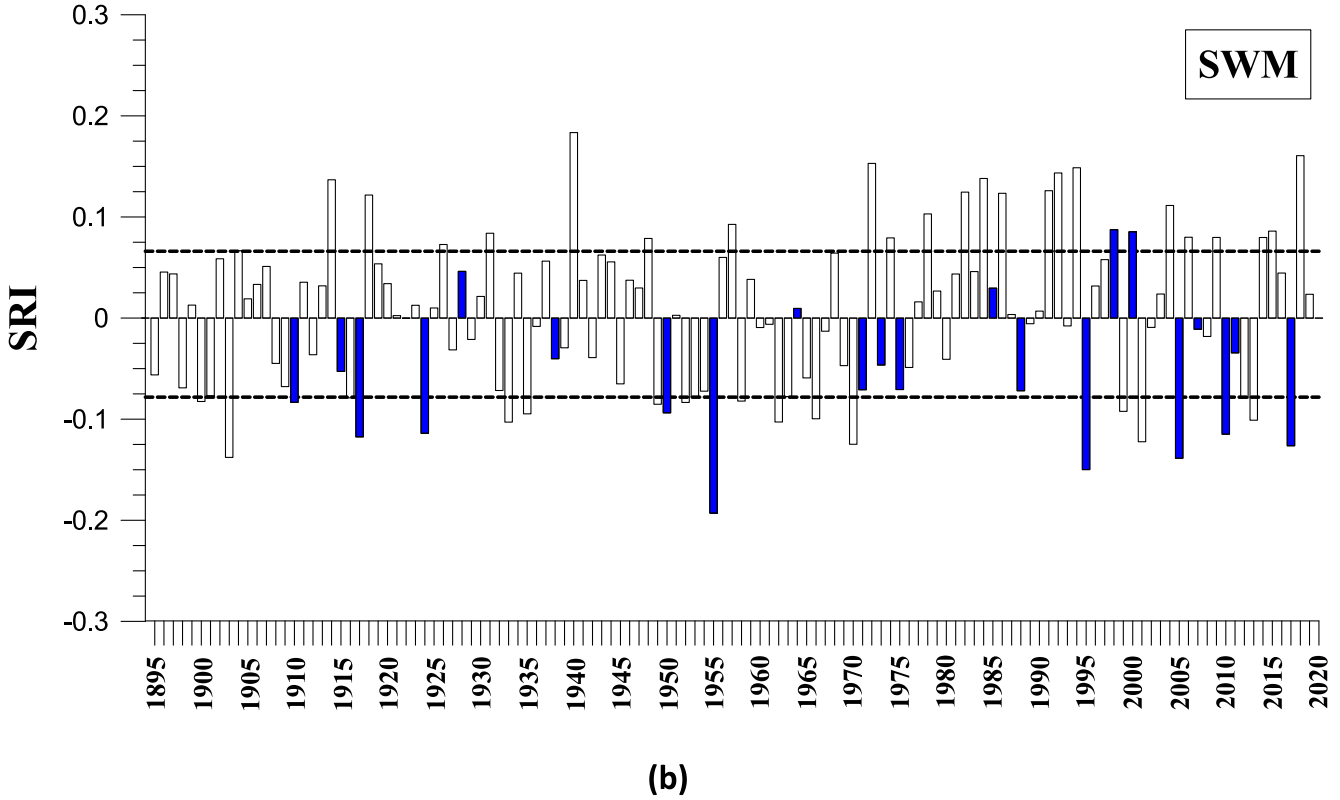

(b)

Fig. 16. As in Fig. 12, except for the candidate SWM region.

Table 3
Properties of the candidate regions (La Niña events).

Region	Season	Coherence	Total Episode	Occurrence Episode	Consistency	Extreme Events
NW	Oct (0) – Feb (+)	0.96	22	17	77 %	12
NC	Aug (0) – Feb (+)	0.94	22	16	73 %	6
NEC	Nov(0) – May (+)	0.94	22	17	77 %	8
SE	Nov(0) – May (+)	0.97	22	18	82 %	8
SWM	Oct (0) – Jun (+)	0.95	22	17	77 %	9

Table 4
Probabilistic assessments for significance level based on the hypergeometric distribution (El Niño events).

Case	Region	N	k	n	m	Probability
I	NW	125	63	29	23	0.000
	NC	125	65	29	21	0.007
	NEC	125	58	29	18	0.027
	SE	125	57	29	22	0.000
	SWM	125	63	29	25	0.000
II	NW	125	25	25	9	0.021
	NC	125	25	25	10	0.006
	NEC	125	25	25	11	0.002
	SE	125	25	25	12	0.000
	SWM	125	25	25	14	0.000

Table 5
As in Table 4, except for La Niña events.

Case	Region	N	k	n	m	Probability
I	NW	125	63	22	17	0.004
	NC	125	67	22	16	0.027
	NEC	125	67	22	17	0.009
	SE	125	59	22	18	0.000
	SWM	125	60	22	17	0.002
II	NW	125	25	25	12	0.000
	NC	125	25	25	6	0.180
	NEC	125	25	25	8	0.055
	SE	125	25	25	8	0.055
	SWM	125	25	25	9	0.021

Alaska, modulates a more active low in the eastern Gulf of Alaska. These La Niña-related atmospheric activities affect the North Pacific seasonal storms shifting toward the northwestern United States. As a result, wetter-than-average patterns are observed over the NW region (Cayan and Peterson, 1989). Douglas and Englehart (1984) investigated the US climate patterns in relation to the 1982–1983 ENSO event and linked the observed wet condition with intensification of a mid-latitude trough in the SWM region of the United States. For the climatological causes for the teleconnection, Cayan and Webb (1992) revealed that the SWM wet conditions during the ENSO years are attributed to the mid-latitude storm displacement by active southerly bringing up moisture-laden air currents from the subtropical Pacific. Additionally, they showed drier-than-normal condition during the La Niña events over the SWM region. Webb and Betancourt (1990) noted that the development of the Aleutian low gives rise to the intensification of the SWM frontal storms at the time of the extreme phase of ENSO. A study by Ely et al. (1992) using sea level geopotential height anomalies associated with hydrologic variation over the SWM region indicated that the dominant storm-producing atmospheric circulation pattern is an anticyclone over the Gulf of Alaska and a cyclone off the California coast. Andrade and Sellers (1988) examined significant changes in tropical cyclogenesis during ENSO episodes considering a possible influence of the presence of warm sea surface temperature off the coast of California and pointed out that these atmospheric changes cause frequent tropical cyclone dissipating over Arizona. Also, they emphasized that during the warm ENSO phase anomalous warm water of the west coast of the SWM region is a driver of the enhanced wet condition in fall and spring seasons, which is the source of energy for the strengthened troughs. This warm water weakens the trade wind inversion caused by sinking air resulting from subtropical high. As a result, the warm water allows more moisture-bearing air to enter over the SWM region. From the perspective of storage effects, the findings of Andrade and Sellers are consistent with the results of the present study in that the positive ENSO-related signal has been detected in fall to spring seasons. In addition, Douglas and Englehart (1981) showed a significant correlation between tropical rainfall index and climate pattern of the SWM region and emphasized that the teleconnection could be explained by the eastward moving low latitude troughs and the corresponding cloudiness. Webb and Betancourt (1990) analyzed simultaneous and lag relationships between climate patterns in the Line Islands and Tucson, Arizona, and pointed out tropical cloud masses moving northeastward from the central tropical Pacific as a driving factor of the significant correlation. This implies that the subtropical jet stream enhanced by the equatorial convection produces more intense storm systems over the SWM region.

Tropical cyclones infiltrating into the region increase and decrease rainstorms but are not the only mechanism responsible for the positive and negative responses during the warm and cold phases of ENSO forcing. Simonson et al. (2022) stated that the occurrence of these climate patterns could be connected with southward shifted storm tracks over the NEC region. The circulation shifts are associated with intensified rainstorms because of southerly wind anomalies and modulate enhanced moisture-laden air transport into the region. The rainfall erosivity response in the southeastern United States to the ENSO phenomena is consistent with Ropelewski and Halpert (1986), Douglas and Englehart (1981). Ropelewski and Halpert (1986) stated that the climate response to ENSO may be more easily explained in terms of direct or shorter-range effects related to the enhanced subtropical jet stream and warmer than normal surface water over the Pacific. Douglas and Englehart (1981) suggested that the ENSO-related climate signal may be an indication of a more direct link to ENSO forcing than a Pacific North American teleconnection pattern (PNA). Active ENSO-related convection is typical in the equatorial Pacific, south of the southeastern United States. This convection has been linked to stronger than normal westerlies in the southern parts of the United States including Gulf of Mexico (e.g., 200 mb ENSO composites in Arkin, 1982) and, hence, a tendency for more frequent storms in the southeastern United States. This possible direct link to the ENSO-related forcing may account for the consistent storm response over the southeastern US. Rasmusson and Wallace (1983) found a strengthened subtropical jet stream displaced southward from its normal position during the mature phases of ENSO event (1982–1983). This pronounced intensification of the jet stream drove numerous seasonal storms causing flooding events in the southern parts of the United States. Additionally, they indicated that this region has shown abnormal wet conditions associated with past ENSO events. The central region is one of regions over the United States in which cloudiness correlates significantly with the sea surface temperature over the tropical Pacific Ocean. Angell and Korshover (1987) employed a combined parameter of sunshine duration and cloud amount as a cloudiness index and identified a significant increase of cloudiness over the NC during 1950 to 1985. They showed that during the warm phase of ENSO forcing cloudiness is 5% above average, while below normal cloudiness exhibits at the time of cold events. During the ENSO event years, the persistent occurrence of warm/cold sea surface temperatures over the

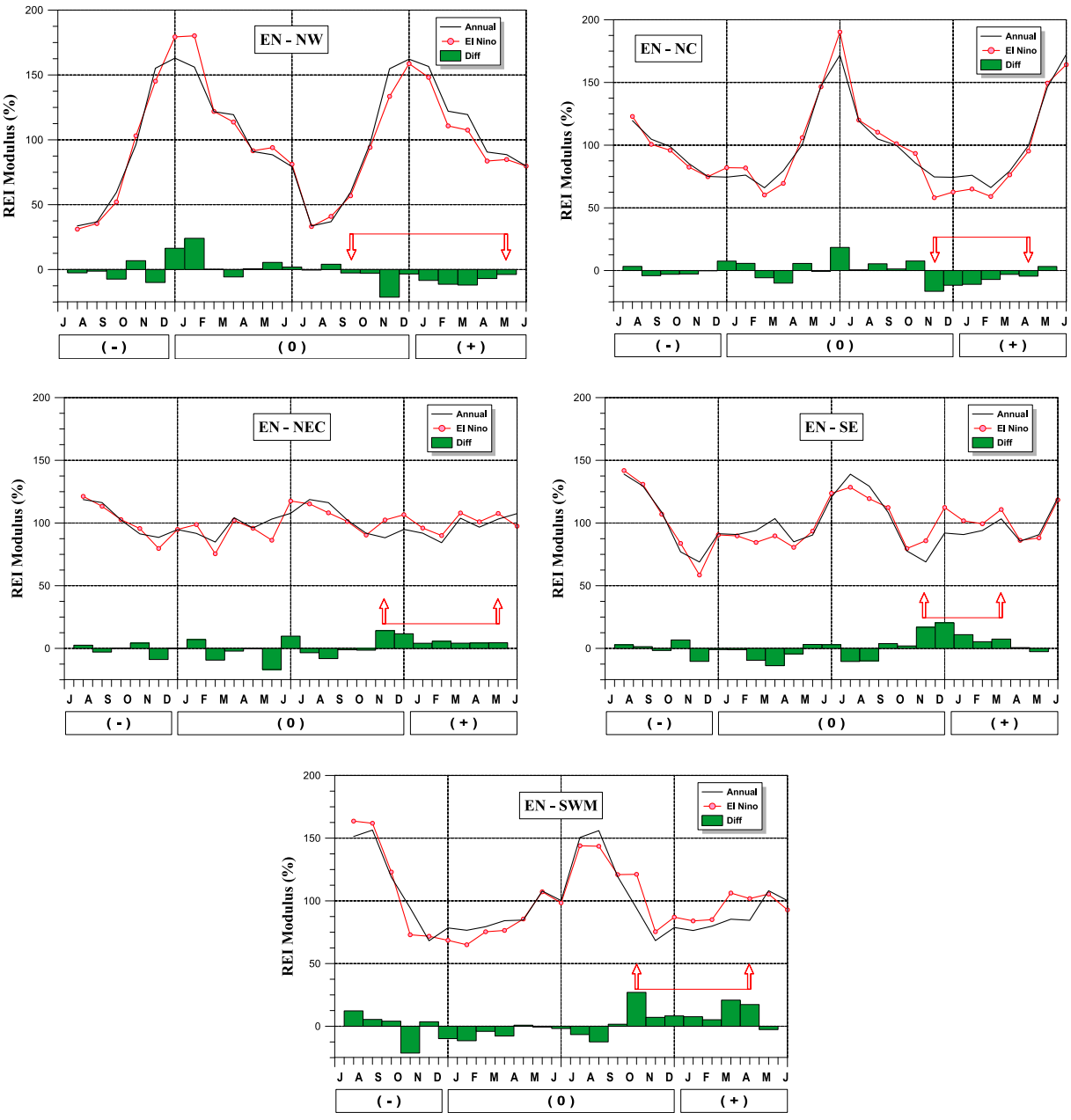

Fig. 17. The comparison between El Niño composite cycles (solid line with circle symbols) and annual cycles of the NW, NC, NEC, SE, and SWM regions, based on modular coefficients. Arrows indicate the beginning and end months of the SO signal season.

central and eastern equatorial Pacific triggers large-scale atmospheric fluctuations in the middle latitude based on complex air-sea coupled interactions. As a result, these ENSO-related middle latitude circulations excite abnormal erosive storm patterns over the United States.

6. Summary and conclusions

Teleconnection between two phases of ENSO thermal forcing and monthly rainfall erosivity anomaly in the United States was investigated using a set of empirical and statistical analyses, such as harmonic analysis, annual cycle composites, and cross-correlation analysis. The details of the general results for ENSO-related REI signals are outlined in Tables 2 to 5. From the results of vectorial mapping through composite and harmonic analyses, the proposed study area is classified into five core regions designated as the northwest (NW), the north central (NC), the northeast coastal (NEC), the southeast (SE), and the southwest/middle-inland (SWM) regions. They showed high levels of spatial coherence and temporal consistency with notable spatial range and amplitude of the rainfall erosivity response to ENSO phenomena. The main conclusions are outlined as follows.

During the El Niño events, the monthly rainfall erosivity anomalies are below normal in the NW and NC regions, and above normal in the NEC, SE, and SWM regions. For the NW and NC regions, the Sep (0) to May (+) and Nov (0) to Apr (+) are the signal seasons showing the noticeable consistency in rainfall erosivity in association with the warm ENSO forcing, and the Nov (0) to May (+), Sep (0) to Mar (+), and Sep (0) to Apr (+) are the signal seasons having a high level of temporal consistency in ENSO-related REI responses for the NEC, SE, and SWM regions, respectively. The spatial coherence of the five core regions for the warm thermal forcing ranges from 0.93 to 0.98 and the temporal consistency are between 0.62 and 0.86. Especially, the SE core region showed the highest magnitude of the positive REI departure for the El

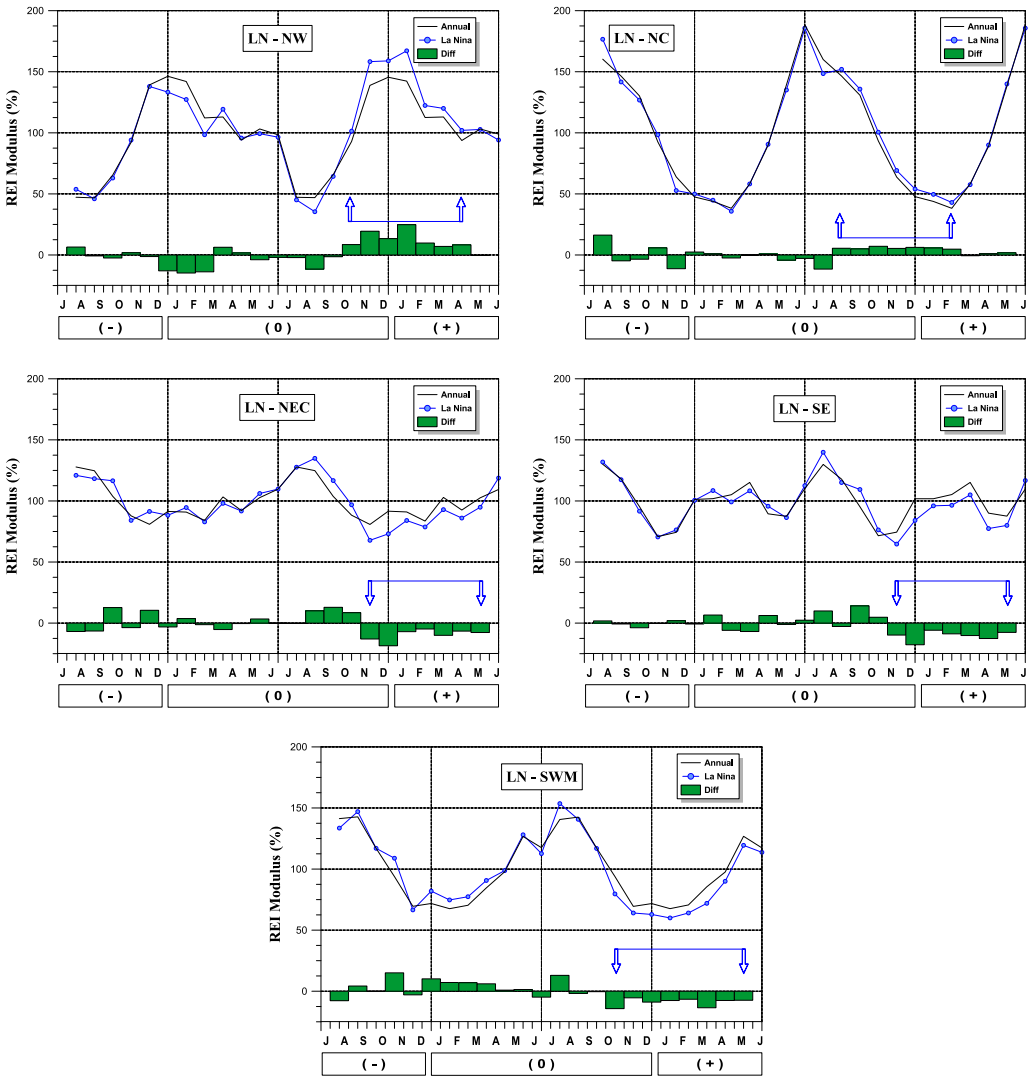

Fig. 18. As in Fig. 17, except for La Niña composite cycles.

Table 6
Cross-correlation coefficients with respect to regions. REI anomalies over NW (NEC and SE) region are correlated with the strong El Niño SOI two to three (one to three) seasons in advance, while REI anomalies over NW, NEC, and SE regions are correlated with the Strong La Niña SOI two to three seasons in advance.

Core Region		Strong El Niño SOI					Normal Condition					Strong La Niña SOI				
		lag-0	lag-1	lag-2	lag-3	lag-4	lag-0	lag-1	lag-2	lag-3	lag-4	lag-0	lag-1	lag-2	lag-3	lag-4
El Niño	NW	−0.08	−0.03	**−0.45**	**−0.43**	−0.15	0.04	0.13	0.06	0.07	−0.02	0.20	0.05	**0.41**	**0.40**	0.02
	NC	−0.10	−0.03	−0.03	−0.02	−0.08	0.06	0.06	−0.04	0.03	−0.05	0.19	0.02	0.21	0.03	0.06
	NEC	0.19	**0.44**	**0.42**	**0.39**	0.18	0.08	0.07	−0.03	0.02	−0.12	−0.08	−0.10	**−0.52**	**−0.41**	−0.26
	SE	0.08	**0.42**	**0.54**	**0.53**	0.11	−0.02	0.02	−0.01	−0.05	−0.02	−0.20	−0.08	**−0.40**	**−0.53**	−0.14
	SWM	0.30	0.04	0.00	0.00	0.11	−0.04	−0.11	−0.12	−0.01	0.02	−0.06	−0.19	−0.08	−0.08	−0.12
La Niña	NW	−0.07	−0.02	**−0.51**	**−0.40**	−0.10	0.04	0.12	0.05	0.06	−0.03	0.20	0.01	**0.42**	**0.46**	0.06
	NC	−0.07	−0.01	−0.02	−0.03	−0.05	0.13	0.04	−0.01	0.05	−0.10	0.21	0.02	0.14	0.01	0.07
	NEC	0.11	**0.43**	**0.40**	**0.41**	0.14	0.10	0.08	−0.03	0.02	−0.12	−0.15	−0.12	**−0.53**	**−0.37**	−0.29
	SE	0.02	**0.41**	**0.52**	**0.42**	0.12	0.00	0.04	0.00	−0.04	−0.01	−0.23	−0.03	**−0.42**	**−0.54**	−0.04
	SWM	0.27	0.01	0.01	0.01	0.12	−0.02	−0.10	−0.07	0.00	0.00	−0.11	−0.14	−0.13	−0.08	−0.15

Niño years. For the La Niña events, the monthly rainfall erosivity anomalies are above normal in NW and NC regions, and below normal in the NEC, SE, and SWM regions. The results of the composite and harmonic analyses show that the signal seasons for positive period are October (0) to February (+) and Aug (0) to Feb (+), and the signal seasons for negative periods are Nov (0) to May (+), Nov (0) to May (+), and Oct (0) to Jun (+) for the NEC, SE, and SWM regions, respectively. The spatial coherence rates for the five core regions for La Niña events range from 0.94 to 0.97, and the temporal consistency for each core region are 0.77 to 0.82.

Comparative analyses of rainfall erosivity responses to both warm and cold ENSO events reveal the high significance level of the ENSO-related REI correlation with an opposite tendency in monthly rainfall erosivity anomalies. The NW and NC regions show negative (positive) tendency for warm (cold) phase, while the NEC, SE, and SWM regions show positive (negative) responses to the warm (cold) phase of ENSO

episode. Above normal rainfall erosivity anomalies during the El Niño thermal forcing are more significant than below normal REI departures during the La Niña events. From the results of annual cycle analysis, the tropical heating and cooling anomalies of sea surface temperature modulate the annual rainfall erosivity cycle over the United States by increasing or decreasing. The highest positive correlation coefficient values are shown in the lag-2 to lag-3 cases over the NW region, and negative correlations are found in the lag-1 to lag-3 cases over the NEC and SE regions for the strong warm phase SOI condition. For the strong cold phase SOI condition, the highest negative correlation coefficient values are found at the NW region with lag-2 to lag-3 cases, and positive correlations are shown at the NEC and SE regions with lag-2 to lag-3 cases. That is, the stronger warm and cold phases of ENSO forcing, the more and less rainfall erosivity with lag time 1 to 3 seasons over the United States. From the findings above, it is concluded that middle latitude rainfall erosivity responses to the El Niño and La Niña phenomena are detectable over the contiguous United States.

Declaration of Competing Interest

The authors declare that they have no known competing financial interests or personal relationships that could have appeared to influence the work reported in this paper.

Data availability

Data will be made available on request.

Appendix A. Supplementary data

Supplementary data to this article can be found online at https://doi.org/10.1016/j.catena.2023.107050.

References

Andrade, E.R., Sellers, W.D., 1988. El Niño and its effect on precipitation in Arizona. J. Clim. 8, 403–410.

Angell, J.K., Korshover, J., 1987. Variability in United States cloudiness and its relation to El Niño. J. Clim. Appl. Meteor. 26, 580–584.

Arkin, P.A., 1982. The relationship between interannual variability in the 200 mb tropical wind field and the Southern Oscillation. Mon. Wea. Rev. 110, 1393–1404.

Berlage, H.P., 1966. The Southern Oscillation and world weather. Meteor. Inst. Meded. Verh. 88, 152 pp.

Cayan, D.R., Peterson, D.H., 1989. The influence of North Pacific atmospheric circulation on streamflow in the West, in Aspects of climate variability in the Pacific and the Western Americas. Amer. Geophys. Union, Monogr. 55, 375–397.

Cayan, D.R., Webb, R.H., 1992. In: El Niño/Southern Oscillation and streamflow in the western United States, in El Niño: Historical and Paleoclimatic Aspects of the Southern Oscillation. Cambridge University Press, pp. 29–68.

Chandimala, J., Zubair, L., 2007. Predictability of streamflow and rainfall based on ENSO for water resources management in Sri Lanka. J. Hydrol. 335, 303–312.

Chiew, F.H.S., McMahon, T.A., Dracup, J.A., Piechota, T., 1994. El Niño/Southern Oscillation and the streamflow patterns in south-east Australia. Civil Eng. Trans., Inst. Eng., Australia CE36 (4), 285–291.

Diaz, H.F., Kiladis, G.N., 1993. In: El Niño/Southern Oscillation and streamflow in the western United States, in El Nitio: Historical and Paleoclimatic Aspects of the Southern Oscillation. Cambridge University Press, pp. 8–28.

Douglas, A.E., Englehart, P.J., 1981. On a statistical relationship between autumn rainfall in the central equatorial pacific and subsequent winter precipitation in Florida. Mon. Weather Rev. 109, 2377–2382.

Douglas, A.E., Englehart, P.J., 1984. Factors leading to the heavy precipitation regimes of 1982–1983 in the United States. Proc. Of the Eighth Annual Climate Diagnostics Workshop. Washington, DC, pp. 42–54.

Ely, L.L., Enzel, Y., Cayan, D.R., 1992. Anomalous atmospheric circulation and large winter floods in six subregions of the Southwestern United States, Proceedings of the Eighth Annual Pacific Climate (PACLIM) Workshop, 179-186.

Emery, W.J., Hamilton, K., 1985. Atmospheric forcing of interannual variability in the northeast Pacific Ocean: Connections with El Niño. J. Geophys. Res. 90, 857–868.

Haan, C.T., 1977. Statistical Methods in Hydrology. Iowa State University Press, Ames, IA.

Hoomehr, S., Schwartz, J., Yoder, D.C., 2015. Potential Change in Rainfall Erosivity under GCM Climate Change Scenarios for the Southern Appalachian Region, USA. Catena 136, 141–151.

Jin, Y.H., Kawamura, A., Jinno, K., Berndtsson, R., 2005. Quantitative relationship between SOI and observed precipitation in southern Korea and Japan by nonparametric approaches. J. Hydrol. 301, 54–65.

Kahya, E., Dracup, J.A., 1993. US streamflow patterns in relation to the El Niño/Southern Oscillation. Water Resour. Res. 29 (8), 2491–2503.

Kahya, E., Dracup, J.A., 1994. The influences of Type 1 El Niño and La Niña events on streamflows in the Pacific southwest of the United States. J. Clim. 7, 965–976.

Kahya, E., Karabörk, M.C., 2001. The analysis of El Niño and La Niña signals in streamflows of Turkey. Int. J. Climatol. 21 (10), 1231–1250.

Kiladis, G.N., Diaz, H.F., 1989. Global climatic anomalies associated with extremes in the Southern Oscillation. J. Climate 2, 1069–1090.

Lee, J.H., Julien, P.Y., 2017. Influence of the El Niño/Southern Oscillation on South Korean streamflow variability. Hydrol. Processes 31 (12), 2162–2178.

Lee, J.H., Lee, J., Julien, P.Y., 2018. Global climate teleconnection with rainfall erosivity in South Korea. Catena 167, 28–43.

Lee, J.H., Yang, C.Y., Julien, P.Y., 2020a. Taiwanese rainfall variability associated with large-scale climate phenomena. Adv. Water Resour. 135, 103462.

Lee, J.H., Julien, P.Y., Thornton, C., 2020b. Large-scale climate teleconnections with South Korean streamflow variability. Hydrol. Sci. J. 65 (1), 57–70.

McKee, T.B., Doesken, N.J., Kleist, J., 1993. The relationship of drought frequency and duration to time series. In: 8th Conference on Applied Climatology, pp. 179–187.

Mohammadi, M., 2015. Rainfall Trends and Their Impacts on Soil Erosion in North Watersheds of Iran. J. Nov. Appl. Sci. 4 (6), 674–681.

Mondal, A., Khare, D., Kundu, S., 2016. Change in Rainfall Erosivity in the Past and Future due to Climate Change in the Central Part of India. Int. Soil Water Conserv. Res. 4 (3), 186–194.

Nearing, M.A., 2001. Potential Changes in Rainfall Erosivity in the U.S. with Climate Change during the 21st century. J. Soil Water Conserv. 56 (3), 229–232.

Nearing, M.A., Pruski, F.F., O'Neal, M.R., 2004. Expected Climate Change Impacts on Soil Erosion Rates: A review. J. Soil Water Conserv. 59 (1), 43–50.

Plangoen, P., Babel, M.S., Clemente, R.S., Shrestha, S., Tripathi, N.K., 2013. Simulating the Impact of Future Land Use and Climate Change on Soil Erosion and Deposition in the Mae Nam Nan Sub-Catchment, Thailand. Sustainability 5, 3244–3274.

Rasmusson, E.M., Carpenter, T.H., 1983. The relationship between eastern equatorial Pacific sea surface temperatures and rainfall over India and Sri Lanka. Mon. Wea. Rev. 111, 517–528.

Rasmusson, E.M., Wallace, J.M., 1983. Meteorological aspects of the El Niño/southern oscillation. Science 222, 1195–1202.

Redmond, K.T., Koch, R.W., 1991. Surface climate and streamflow variability in the western United States and their relationship to large circulation indices. Water Resour. Res., 27(9), 2381–2399, 1991.

Ropelewski, C.F., Halpert, M.S., 1986. North American precipitation and temperature patterns associated with El-Niño-Southern oscillation (ENSO). Mon. Weather Rev. 114, 2165–2352.

Ropelewski, C.F., Halpert, M.S., 1987. Global and regional scale precipitation patterns associated with the El Niño/Southern Oscillation. Mon. Wea. Rev. 115, 1606–1626.

Ropelewski, C.F., Halpert, M.S., 1989. Precipitation patterns associated with the high index phase of the southern oscillation. J. Clim. 2, 268–284.

Shiono, T., Ogawa, S., Miyamoto, T., Kameyama, K., 2013. Expected Impacts of Climate Change on Rainfall Erosivity of Farmlands in Japan. Ecol. Eng. 61, 678–689.

Simonson, J.M., Birkel, S.D., Maasch, K.A., Mayewski, P.A., Lyon, B., Carleton, A.M., 2022. Association between recent U.S. northeast precipitation trends and Greenland blocking. Int. J. Climatol. 42 (11), 5682–5693.

Walker, G.T., 1923. Correlation in seasonal variations of weather, V III, A preliminary study of world weather. Mem. Indian Meteorol. Dep. 24, 75–131.

Walker, G.T., Bliss, E.W., 1932. World Weather V. Mem. Roy. Meteor. Soc. 4 (36), 53–84.

Wang, L., Yang, Z., Gu, X., Li, J., 2020. Linkages Between Tropical Cyclones and Extreme Precipitation over China and the Role of ENSO. Int. J. Disaster Risk Sci. 11, 538–553.

Webb, R.H., Betancourt, J.L., 1990. Climatic effects on flood frequency: An example from southern Arizona. In: Proceeding of the Sixth Annual Pacific Climate (PACLIM) Workshop, report. California State Dept. of Water Resources, Sacramento, pp. 61–66.

Westra, S., Alexander, L.V., Zwiers, F.W., 2013. Global increasing trends in annual maximum daily precipitation. J. Clim. 26, 3904–3918.

Wilks, D.S., 1995. Statistical Methods in Atmospheric Sciences. Academic Press 330–334.

WMO, 2014. El Niño/Southern Oscillation. WMO-No. 1145, 2–4.

Yang, D., Kanae, S., Oki, T., Koike, T., Musiake, K., 2003. Global Potential Soil Erosion with Reference to Land Use and Climate Changes. Hydrol. Process. 17, 2913–2928.

Yang, X., Bofu, Y., Xiaojin, X., 2015. Predicting Changes of Rainfall Erosivity and Hillslope Erosion Risk across Greater Sydney Region, Australia., International Journal of Geospatial and Environmental Research, Vol.2(1), Article 2. http://dc.uwm.edu/ijger/vol2/iss1/2.

Zhang, G.H., Nearing, M.A., Liu, B.Y., 2005. Potential effects of climate change on rainfall erosivity in the Yellow River basin of China.Trans. Trans. ASAE 48 (2), 511–517.